



**NAVAL  
POSTGRADUATE  
SCHOOL**

**MONTEREY, CALIFORNIA**

**THESIS**

**DESIGN AND OPTIMIZATION OF COPPER INDIUM  
GALLIUM SELENIDE THIN FILM SOLAR CELLS**

by

Daniel B. Katzman

September 2015

Thesis Advisor:  
Second Reader:

Sherif Michael  
Matthew Porter

**Approved for public release; distribution is unlimited**

THIS PAGE INTENTIONALLY LEFT BLANK

REPORT DOCUMENTATION PAGE			Form Approved OMB No. 0704-0188	
Public reporting burden for this collection of information is estimated to average 1 hour per response, including the time for reviewing instruction, searching existing data sources, gathering and maintaining the data needed, and completing and reviewing the collection of information. Send comments regarding this burden estimate or any other aspect of this collection of information, including suggestions for reducing this burden, to Washington headquarters Services, Directorate for Information Operations and Reports, 1215 Jefferson Davis Highway, Suite 1204, Arlington, VA 22202-4302, and to the Office of Management and Budget, Paperwork Reduction Project (0704-0188) Washington, DC 20503.				
1. AGENCY USE ONLY (Leave blank)		2. REPORT DATE September 2015	3. REPORT TYPE AND DATES COVERED Master's Thesis	
4. TITLE AND SUBTITLE DESIGN AND OPTIMIZATION OF COPPER INDIUM GALLIUM SELENIDE THIN FILM SOLAR CELLS			5. FUNDING NUMBERS	
6. AUTHOR(S) Katzman, Daniel B.				
7. PERFORMING ORGANIZATION NAME(S) AND ADDRESS(ES) Naval Postgraduate School Monterey, CA 93943-5000			8. PERFORMING ORGANIZATION REPORT NUMBER	
9. SPONSORING /MONITORING AGENCY NAME(S) AND ADDRESS(ES) N/A			10. SPONSORING/MONITORING AGENCY REPORT NUMBER	
11. SUPPLEMENTARY NOTES The views expressed in this thesis are those of the author and do not reflect the official policy or position of the Department of Defense or the U.S. Government. IRB Protocol number ___N/A___.				
12a. DISTRIBUTION / AVAILABILITY STATEMENT Approved for public release; distribution is unlimited			12b. DISTRIBUTION CODE	
13. ABSTRACT (maximum 200 words)  The objective of this thesis was to simulate a new way to create high efficiency Copper Indium Gallium Selenide (Cu(InGa)Se <sub>2</sub> ) cells. This was accomplished by creating a model in Silvaco's technology computer aided design ATLAS program. A baseline model was tested to confirm functionality of the software, and a stepwise approach was used to include additional features. The first addition was the inclusion of a multi-layer absorber layer with graded Ga concentrations. This layer showed increased internal electric fields, which helped to increase the output of the cell. This was followed by the replacement of the traditional <i>n</i> -type CdS buffer layer with a <i>n</i> -type ZnO buffer layer. The ZnO buffer layer was found to have better band alignment than CdS and resulted in a significant improvement in device performance. Finally, a top grid was included which reduced the output of the cell as a result of shading. The final simulation resulted in a Cu(InGa)Se <sub>2</sub> cell which operated at 21.14% efficiency, a 21.9% increase from the baseline cell.				
14. SUBJECT TERMS CIGS, efficiency, solar, SILVACO, ATLAS			15. NUMBER OF PAGES 71	
			16. PRICE CODE	
17. SECURITY CLASSIFICATION OF REPORT Unclassified	18. SECURITY CLASSIFICATION OF THIS PAGE Unclassified	19. SECURITY CLASSIFICATION OF ABSTRACT Unclassified	20. LIMITATION OF ABSTRACT UU	

THIS PAGE INTENTIONALLY LEFT BLANK

**Approved for public release; distribution is unlimited**

**DESIGN AND OPTIMIZATION OF COPPER INDIUM GALLIUM SELENIDE  
THIN FILM SOLAR CELLS**

Daniel B. Katzman  
Captain, United States Marine Corps  
B.S.E., University of Michigan, 2007

Submitted in partial fulfillment of the  
requirements for the degree of

**MASTER OF SCIENCE IN ELECTRICAL ENGINEERING**

from the

**NAVAL POSTGRADUATE SCHOOL  
September 2015**

Author: Daniel B. Katzman

Approved by: Sherif Michael  
Thesis Advisor

Matthew Porter  
Second Reader

Ralph Robertson  
Chair, Department of Electrical and Computer Engineering

THIS PAGE INTENTIONALLY LEFT BLANK

## ABSTRACT

The objective of this thesis was to simulate a new way to create high efficiency Copper Indium Gallium Selenide ( $\text{Cu(InGa)Se}_2$ ) cells. This was accomplished by creating a model in Silvaco's technology computer aided design ATLAS program. A baseline model was tested to confirm functionality of the software, and a stepwise approach was used to include additional features. The first addition was the inclusion of a multi-layer absorber layer with graded Ga concentrations. This layer showed increased internal electric fields, which helped to increase the output of the cell. This was followed by the replacement of the traditional  $n$ -type CdS buffer layer with a  $n$ -type ZnO buffer layer. The ZnO buffer layer was found to have better band alignment than CdS and resulted in a significant improvement in device performance. Finally, a top grid was included which reduced the output of the cell as a result of shading. The final simulation resulted in a  $\text{Cu(InGa)Se}_2$  cell which operated at 21.14% efficiency, a 21.9% increase from the baseline cell.

THIS PAGE INTENTIONALLY LEFT BLANK

# TABLE OF CONTENTS

I.	INTRODUCTION.....	1
A.	BACKGROUND .....	1
B.	THESIS OBJECTIVE .....	4
C.	APPROACH.....	5
D.	THESIS OUTLINE.....	5
II.	BACKGROUND .....	7
A.	SOLAR CELL PHYSICS .....	7
1.	Solar Spectrum and Wavelength Energy .....	7
2.	Photogeneration of Electron Hole Pairs .....	8
3.	Solar Cell Current Voltage Characteristics .....	9
a.	<i>Short-Circuit Current</i> .....	9
b.	<i>Open-Circuit Voltage</i> .....	11
c.	<i>Solar Cell Characteristics</i> .....	11
4.	Non-ideal Factors in Solar Cell Characteristics.....	12
a.	<i>Trap Assisted Recombination</i> .....	12
b.	<i>Contact Shading</i> .....	13
c.	<i>Temperature Effects</i> .....	14
d.	<i>Back Surface Field</i> .....	14
e.	<i>Other Factors that Degrade Performance</i> .....	15
B.	CU(INGA)SE <sub>2</sub> SOLAR CELLS.....	15
1.	n-CdS/Cu(InGa)Se <sub>2</sub> Solar Cell Design .....	16
2.	Developments in Cu(InGa)Se <sub>2</sub> Design.....	18
C.	TRAP DENSITY IN CIGS ALLOYS .....	19
III.	TCAD MODELING OF Cu(InGa)Se <sub>2</sub> CELLS.....	23
A.	SILVACO ATLAS INTRODUCTION.....	23
B.	ATLAS FUNCTION.....	24
1.	Poisson's Equation .....	25
2.	Transport Equations.....	26
3.	Continuity Equations.....	26
C.	ATLAS OUTPUT.....	26
D.	INITIAL MODEL DEVELOPMENT .....	27
IV.	SIMULATION AND RESULTS .....	29
A.	SINGLE ABSORBER LAYER .....	29
B.	DUAL-GRADED ABSORBER LAYER .....	31

C.	TRAPEZOIDAL ABSORBER LAYER .....	35
D.	ALTERNATE BUFFER LAYER.....	37
E.	TOP GRID.....	40
V.	CONCLUSIONS AND RECOMMENDATIONS.....	43
A.	CONCLUSIONS .....	43
B.	RECOMMENDATIONS FOR FUTURE WORK.....	44
	APPENDIX. SILVACO CODE .....	45
	LIST OF REFERENCES.....	49
	INITIAL DISTRIBUTION LIST .....	53

## LIST OF FIGURES

Figure 1.	Global resource map showing solar intensity, from [4].	2
Figure 2.	GREENS setup in support of a Marine artillery unit, from [6].	3
Figure 3.	SPACES being used by Marines in Afghanistan, from [8].	4
Figure 4.	Solar irradiance spectrum breakdowns for various classifications, from [12].	7
Figure 5.	Illustration of photo generation and recombination, from [12].	9
Figure 6.	Sample solar cell IV curve, from [15].	12
Figure 7.	Illustration of defect trap recombination process, from [16].	13
Figure 8.	Colorized scanning electron microscope image of Cu(InGa)Se <sub>2</sub> structure, from [19].	16
Figure 9.	Band structure for Cu(InGa)Se <sub>2</sub> solar cell, from [20].	17
Figure 10.	Plot of defect concentration versus Ga composition, from [25].	20
Figure 11.	Average defect concentration as a function of Ga composition, from [26].	21
Figure 12.	Basic Cu(InGa)Se <sub>2</sub> cell structure file showing mesh.	25
Figure 13.	Structure output showing electric-field strength for baseline cell.	29
Figure 14.	Family of IV curves for single-graded absorber layer simulations.	30
Figure 15.	Single-absorber layer efficiencies plotted as a function of slope.	31
Figure 16.	Example mole fraction profile for a dual-graded absorber layer.	32
Figure 17.	Dual-absorber layer efficiencies plotted as a function of slope.	33
Figure 18.	Structure output showing electric-field strength for an ungraded absorber.	34
Figure 19.	Structure output showing electric-field strength for a graded absorber.	35
Figure 20.	Example mole fraction profile for a trapezoidal absorber layer.	36
Figure 21.	Structure output showing electric-field strength for trapezoidal-graded absorber.	36
Figure 22.	Trapezoidal absorber layer efficiencies plotted as a function of slope.	37
Figure 23.	Band diagram for a cell with a CdS buffer layer.	38
Figure 24.	Band diagram for a cell with a ZnO buffer layer.	39
Figure 25.	ZnO buffer layer efficiencies plotted as a function of thickness.	40
Figure 26.	Photogeneration plot for a cell without a top contact grid.	41
Figure 27.	Photogeneration plot for a cell with a top contact grid.	42

THIS PAGE INTENTIONALLY LEFT BLANK

**LIST OF TABLES**

Table 1. Variable definitions for current density equation. ....10

THIS PAGE INTENTIONALLY LEFT BLANK

## LIST OF ACRONYMS AND ABBREVIATIONS

CInSe <sub>2</sub>	Copper Indium Diselenide
Cu(InGa)Se <sub>2</sub>	Copper Indium Gallium Selenide
CGaSe <sub>2</sub>	Copper Gallium Diselenide
DOD	Department of Defense
E2O	Expeditionary Energy Office
GREENS	Ground Renewable Expeditionary Energy System
NPS	Naval Postgraduate School
SPACES	Solar Portable Alternative Communications Energy System
TCAD	Technology Aided Computer Design

THIS PAGE INTENTIONALLY LEFT BLANK

## **ACKNOWLEDGMENTS**

I would like to start by thanking my advisor, Professor Sherif Michael. His guidance and tutelage during this process has been invaluable. I would also like to thank my second reader, Matthew Porter. His knowledge and expertise both in semiconductor physics and with the SILVACO ATLAS software guided me toward successfully completing this thesis and rounded out my educational experience.

THIS PAGE INTENTIONALLY LEFT BLANK

# I. INTRODUCTION

## A. BACKGROUND

The Department of Defense (DOD) created the Office of the Assistant Secretary of Defense for Operational Security in 2010. The mission of this office is “to help the military services and combatant command improve military capabilities, cut costs, and lower operational and strategic risk through better energy accounting, planning, management, and innovation” [1].

As part of the overall scheme to improve the DOD’s operational energy usage, this office published its Operational Energy Strategy in 2011. Within the strategy, three principals were outlined to serve as the focal points for the office’s efforts. The first principle is more fight, less fuel [2]. The intent of this principle is to reduce the reliance of the DOD on fossil fuels as much as possible. The second principle is to have more options while assuming less risk. This principle focuses on increasing the available energy production options while reducing the dependence on any one source, avoiding the risk of a single point of failure. The third principle is to develop more capability at a lower cost through reducing energy procurement expenditures [2]. To aid this effort, the United States Marine Corps created the Expeditionary Energy Office (E2O) in 2009 as part of its overall strategy to meet future energy requirements of the force. This office serves as the focal point for the advancement and implementation of the USMC’s expeditionary energy strategy, as laid out in guidance published by the Commandant of the Marine Corps. E2O’s mission is to “analyze, develop, and direct the Marine Corps’ energy strategy in order to optimize expeditionary capabilities across all warfighting functions” [3].

While several strategies are being pursued to meet this vision for future energy provision, solar power stands out as an attractive option. While other sources are being researched, solar power is significantly more consistent and easier to harvest than other options, such as wind. Solar power’s availability in littoral areas where the Marine Corps

operates makes it the ideal choice for an alternate energy source, as illustrated by the map in Figure 1.

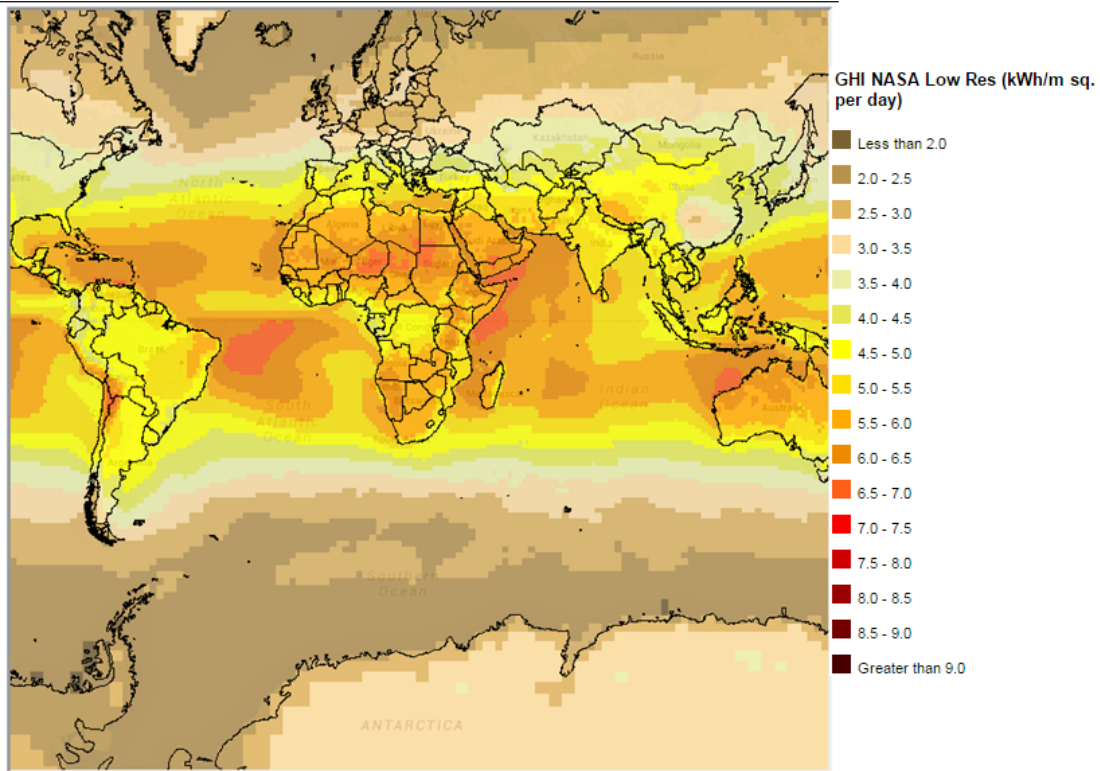


Figure 1. Global resource map showing solar intensity, from [4].

The Marine Corps has already fielded multiple systems aimed at taking advantage of the solar energy that can be harvested where it conducts a majority of its operations. The largest of these currently in use is the Ground Renewable Expeditionary Energy System (GREENS). GREENS is an expeditionary energy system designed to support units in the field, reducing or eliminating the requirements to run generators to provide power [5]. The energy system is rated at providing 300 W of continuous power that is generated from a set of solar panels rated at 1.6 kW and includes a set of batteries that store the power for non-daylight hours [5]. The use of the GREENS system is illustrated in Figure 2.



Figure 2. GREENS setup in support of a Marine artillery unit, from [6].

The second, more common system currently in use is the Solar Portable Alternative Communications Energy System (SPACES). SPACES is a portable solar cell blanket that has been fielded by the Marine Corps in order to provide access to solar power in a foot mobile package. This system is designed to provide 62 W of power, primarily intended for charging batteries. This equipment allows patrols to significantly decrease the weight they are required to carry. An example of the implementation of SPACES can be seen in Figure 3. Despite the manufacturer's claims, the device's actual output has been measured and found lower than the rated capacity [7]. Better alternatives must be identified and investigated in order to find a viable solution for the future.



Figure 3. SPACES being used by Marines in Afghanistan, from [8].

## **B. THESIS OBJECTIVE**

The objective of this research is to simulate and optimize the design of a new type of Copper Indium Gallium Selenide ( $\text{Cu(InGa)Se}_2$ ) cell, specifically using inhomogeneous  $\text{Cu(InGa)Se}_2$  heterojunctions with absorber layers containing graded mole fractions, advancing previous work completed at the Naval Postgraduate School (NPS) [9]. Broadly, the goal is to research new technology that promises to increase the efficiency of solar cells built using  $\text{Cu(InGa)Se}_2$ . Increasing the efficiency and, therefore, output of solar cells will help equipment such as GREENS and SPACES more effectively support future operations.

### **C. APPROACH**

A summary of research literature discussing the pertinent science and physics behind semiconductors and solar cells is discussed first. Using SILVACO's technology aided computer design (TCAD) ATLAS program, we created and analyzed a model of a thin film Cu(InGa)Se<sub>2</sub> solar cell. Building on a foundation of work previously completed by students at the NPS that simulated Cu(InGa)Se<sub>2</sub> solar cells in various ways [9], [10], we created a basic model which can be modified to incorporate desired features. The latest, most accurate information available should be incorporated into follow-on models to ensure that this work properly accounts for the true behavior of its component materials.

### **D. THESIS OUTLINE**

This thesis is organized as follows. Background information, including solar cells and pertinent physics, are introduced and discussed in Chapter II. In Chapter III, the software to be used for simulation as well as development of the model are discussed. In Chapter IV, the simulations and an analysis of the output and results are discussed. Finally, in Chapter V, conclusions as well as recommendations for future work are provided.

THIS PAGE INTENTIONALLY LEFT BLANK

## II. BACKGROUND

### A. SOLAR CELL PHYSICS

Solar cells are semiconductor devices that rely on the absorption of light, specifically photons, from the solar spectrum to generate electron-hole pairs. The separation and subsequent collection of these electron-hole pairs is the method by which solar cells convert solar energy into useful electricity. In order to create a new solar cell design, a thorough understanding of the underlying science and physics is a requirement.

#### 1. Solar Spectrum and Wavelength Energy

There are multiple standard spectrum classifications used in the study of solar cells. The first, AM0, is the solar spectrum observed in space. It has the widest range of wavelengths and contains approximately 1.4 kW per meter squared ( $\text{kW/m}^2$ ) of solar energy available for absorption [11]. When examining terrestrial applications of solar cells, AM1.5 is the predominant standard used for analysis and simulation. It has a slightly different profile than AM0, as observed in Figure 4.

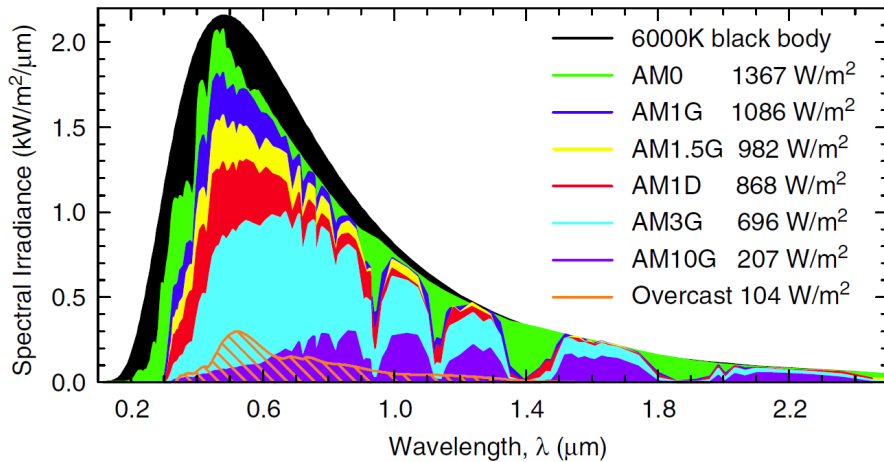


Figure 4. Solar irradiance spectrum breakdowns for various classifications, from [12].

Most of the differences between the spectra are a result of water present in the atmosphere that absorbs some of the available photons as they radiate to the Earth's

surface. The result is fewer photons available for solar cells to convert to usable energy, a reduction to approximately 1 kW/m<sup>2</sup> [11]. Given a fixed amount of input energy, this makes the advancement of solar cells that increase efficiency or take advantage of a larger percentage of these photons necessary.

Once the solar spectrum is understood, the characteristics of photons must be considered. The most important photon characteristic is the wavelength of the photon. Each wavelength corresponds to a specific energy possessed by a given photon. This relationship is demonstrated by

$$E = \frac{1.24}{\lambda} \quad (1)$$

where  $E$  is energy in electron volts and  $\lambda$  is wavelength in micrometers.

From Equation (1), we see that longer wavelength photons contain less energy relative to shorter wavelength photons. Furthermore, photons of longer wavelengths have the ability to penetrate further into a solar cell than those with shorter wavelength. This must be considered when constructing solar cells that have the ability to absorb photons with varying energy levels, such as multi-junction solar cells or graded band-gap solar cells.

## **2. Photogeneration of Electron Hole Pairs**

In order to create an electron-hole pair to generate power, a photon must displace a valence electron from a bond inside of the crystalline structure of the solar cell. The energy required to create these electron-hole pairs are determined by the bandgap of the semiconductor absorber material. If the photon's energy is less than the bandgap of the absorber, it is unable to generate an electron-hole pair and either passes through the material or is absorbed as heat. If the photon has energy higher than the bandgap, it may generate an electron-hole pair, but the additional energy beyond the bandgap is eventually dissipated as heat within the solar cell as the electron settles back to the conduction band. Photogeneration is illustrated in Figure 5.

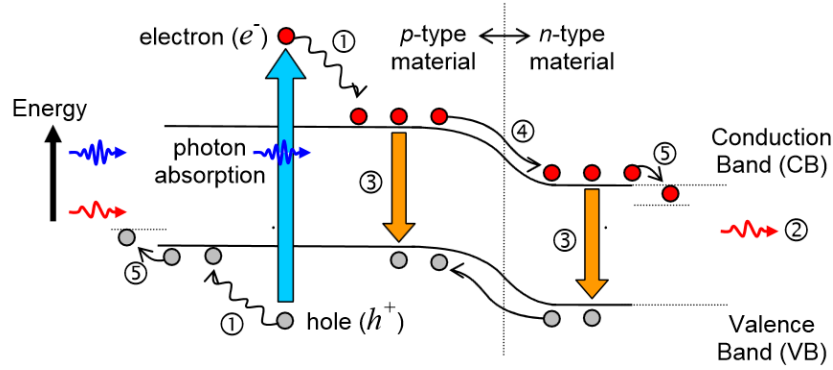


Figure 5. Illustration of photo generation and recombination, from [12].

Once an electron-hole pair is created, it is necessary to move these individual carriers to one of the two contacts on the solar cell in order to harvest them before recombination can occur. The electric field that exists within the materials and junctions helps to sweep these carriers away from each other and towards the contact.

### 3. Solar Cell Current Voltage Characteristics

There are several important physical principles behind the function of solar cells that are important to understanding how and why they work. The result of the photogeneration caused by exposure of solar cells to sunlight is the creation of a voltage potential and a current within the cell. A solar cell is much like a diode as upon exposure to light it conducts in one particular direction, and when the exposure ceases, the diode stops conducting. These voltage and current responses of solar cells are guided by characteristics of each individual solar cell.

#### a. Short-Circuit Current

The current in a solar cell is determined by several factors and the ideal current  $I$  expression is expressed by [13]

$$I = I_s \left( e^{qV/kT} - 1 \right) - I_L \quad (2)$$

where  $I_s$  is the diode saturation current,  $q$  is charge,  $V$  is the voltage of the cell,  $k$  is Boltzmann's constant,  $T$  is temperature and  $I_L$  is the photogeneration current. From

Equation (2), it can be seen that the open circuit current  $I_{OC}$  is equal to  $I_L$  since the exponential term becomes zero when there is no voltage across the device [13].

Expanding on Equation (2), the saturation current density  $J_s$  can be expressed by [13]

$$J_s = qN_c N_v \left( \frac{1}{N_A} \sqrt{\frac{D_n}{\tau_n}} + \frac{1}{N_D} \sqrt{\frac{D_p}{\tau_p}} \right) \bullet e^{\frac{-E_g}{kT}} \quad (3)$$

where the variables for Equation 3 are defined in Table 1.

Table 1. Variable definitions for current density equation.

Variable	Definition
$E_g$	Bandgap
$N_c$	Density of states in conduction band
$N_v$	Density of states in valence band
$N_A$	Acceptor doping
$N_D$	Donor doping
$D_n$	Electron diffusion constant
$D_p$	Hole diffusion constant
$\tau_n$	Electron lifetime
$\tau_p$	Hole lifetime

Typically,  $I_L$  is significantly larger than  $I_s$  and plays a much larger role in characterizing a solar cell. The photogeneration current density  $J_L$  is [14]

$$J_L = qG(L_n + W + L_p) \quad (4)$$

where  $G$  is the generation rate,  $L$  is the diffusion length, and  $W$  is the depletion width. The generation rate is determined by the intensity of the illumination that the solar cell is exposed to. The diffusion lengths  $L$  can be further defined by

$$L_n = \sqrt{D_n \tau_n} \quad (5)$$

and

$$L_p = \sqrt{D_p \tau_p}. \quad (6)$$

From Equations (5) and (6), it can be seen that with a longer carrier lifetime and, therefore, longer diffusion length, the photogeneration current is increased.

**b. Open-Circuit Voltage**

After a thorough analysis of the current, the voltage  $V$  in a solar cell is determined by [13]

$$I = \frac{-V}{R_L} \quad (7)$$

where  $R_L$  is load resistance applied to the output of the solar cell. Guided by this relationship, Equation (2) can be solved for voltage when the current is equal to zero, which results in the open circuit voltage  $V_{oc}$  being expressed as [13]

$$V_{oc} = \frac{kT}{q} \left( \frac{I_L}{I_S} + 1 \right). \quad (8)$$

**c. Solar Cell Characteristics**

When conducting simulations and measurements of solar cells, the desired outputs are the current-voltage (IV) characteristics of the anode voltage of the device versus the cathode current. The effective photogeneration of power is demonstrated by a significantly larger area under the curve when compared to non-illuminated conditions. This is typically completed by sweeping the anode voltage from zero volts to a predetermined maximum voltage. This maximum voltage varies between solar cells and is determined by the properties of the semiconductor materials that make up the cell. This curve demonstrates the behavior of the cell as it operates from its short circuit current to its open circuit voltage as demonstrated in Figure 6.

From the IV curve, there are two important factors that are typically calculated. Once the curve has been produced, the efficiency  $\eta$  is calculated

$$\eta = \frac{P_{out}}{P_{in}} \quad (9)$$

where  $P_{out}$  is the maximum output power and  $P_{in}$  is the input power. The input power is determined by the area of the solar cell and the solar spectrum to which it is exposed. The maximum power is taken from the “knee” of the IV curve, where the product of the current and voltage is maximized as demonstrated in Figure 6. The output power is

calculated from  $P_{out} = V_{mp} I_{mp}$  where  $V_{mp}$  is the maximum power point voltage and  $I_{mp}$  is the maximum power current.

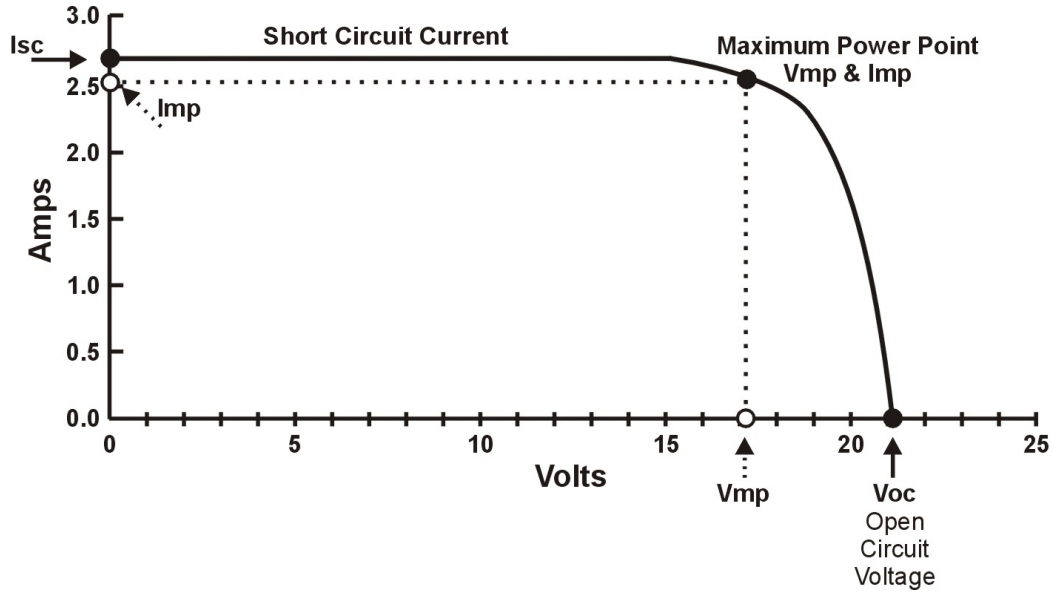


Figure 6. Sample solar cell IV curve, from [15].

The second factor that is typically measured and reported is the fill factor. The fill factor  $FF$  is calculated from

$$FF = \frac{V_{mp} I_{MP}}{V_{OC} I_{SC}}. \quad (10)$$

Fill factor can be a maximum of 100%, and reductions are from a result of internal characteristics of the cell. The higher the fill factor, the more these internal factors have been reduced and the sharper the IV curve appears.

#### 4. Non-ideal Factors in Solar Cell Characteristics

There are several other factors that play a role in the performance of a solar cell that require discussion to ensure a thorough analysis.

##### a. Trap Assisted Recombination

Recombination occurs when an electron from the conduction band and a hole from the valence band recombine, reducing the number of free carriers available within

the semiconductor. This is especially detractive for solar cells because it reduces the number of carriers that can be harvested and turned into useful energy. Defects in solar cell materials can lead to traps which serve as recombination centers that reduce the output of the cell. Traps have an associated energy which dictates a forbidden energy level between the conduction band and the valence band where the carriers can be trapped. In addition, traps have a cross-sectional area where a higher value results in a higher probability of trapping a carrier. Finally, trap density plays a large role in the recombination rate since carrier lifetime decreases as trap density increases. Trap assisted recombination is illustrated in Figure 7.

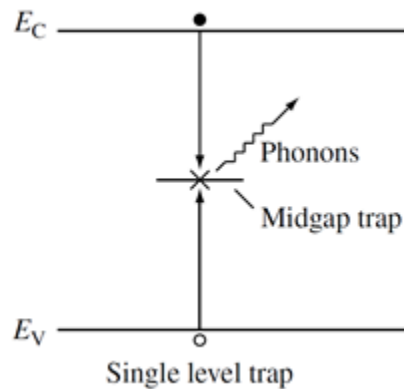


Figure 7. Illustration of defect trap recombination process, from [16].

### ***b. Contact Shading***

In order to harvest the electron-hole pairs generated by the photons absorbed in the solar cells, top and bottom contacts must be included. The bottom contact serves as the anode and can also serve to reflect photons that have penetrated all the way through the absorber layer to increase the output of the cell. The bottom contact typically does not detract from the performance of the solar cell.

The top contact serves as the cathode and is placed on top of the cell. The placement of a metal top contact, which reflects rather than passes photons, creates shading of the solar cell and has a significant impact on the output of the cell [17]. This

results in a desire to reduce the area which is covered by the top contact, but a reduced coverage of top contacts results in a reduced ability to collect carriers.

In an attempt to reduce the shading, a thinner metal contact can be used, but the reduction in cross-sectional area increases the resistance of the top contact grid, effectively reducing the overall output of the cell more than the shading resulting from the top contacts. This requires the balancing of all of these factors to maximize the output of the cell. Overall, an estimated 10% of the top area of a cell is covered by a top grid that results in shading in order to efficiently harvest the energy created by the solar cell [17].

### *c. Temperature Effects*

Temperature plays a large role in the output of a solar cell. For nearly all research, attempts are made in simulations and testing to hold the cell temperature at 25 C. While this makes it easy to conduct a comparison between solar cells, it creates an unrealistic expectation of true device performance. As a result of being exposed to the sun and the absorption of photons, the operating temperature of solar cells increases during exposure. Typical uncooled solar cells tend to operate at temperatures near 50 C; though the actual operating temperature depends on several factors, including ambient temperature, wind speed, etc. This increase in temperature results in a decrease in the output voltage of the solar cell. This results in an output voltage decrease of 2.0 mV per degree [18], meaning that a solar cell operating at 50 C vice 25 C has a resulting 50.0 mV output voltage decrease. This decrease in output voltage can result in up to a 10% decrease in the output of the cell resulting from the higher operating temperature.

### *d. Back Surface Field*

As discussed earlier, recombination plays a large role in the reduction of solar cell output and efficiency. Recombination occurs throughout the solar cell, with significant recombination sites being located at the top and bottom contacts of the cell. Some of this recombination can be reduced through the creation of a back surface field within the solar cell. A back surface field can be created by increasing the doping near the back contact. The back surface field serves to create an additional small electric field that helps to

separate carriers, allowing for their collection and reducing recombination at the back contact.

*e. Other Factors that Degrade Performance*

Reflection off of the top surface of the solar cell is another cause for degraded performance of solar cells. There has been much research on this topic, and it is standard for solar cells to be manufactured with an anti-reflective coating that reduces the number of photons that are reflected, resulting in the increased performance of the cell.

Another significant factor is the internal resistance of the cell. Since the cell is constructed of several different layers, each with its own electrical properties, the layers combine to create an internal resistance to the flow of electricity. Contributing factors include the ohmic contact between semiconductors and metal contacts, and the equivalent resistance of the contacts as well as the inherent resistance associated with the semiconductor materials used in the device.

**B. CU(INGA)SE<sub>2</sub> SOLAR CELLS**

Cu(InGa)Se<sub>2</sub> is an alloy of copper indium diselenide (CInSe<sub>2</sub>) and copper gallium diselenide (CGaSe<sub>2</sub>) which results in a material with characteristics interpolated between both components. The resulting material has a tunable bandgap depending on the mole fraction of Ga, where the mole fraction is calculated from

$$x = \frac{Ga}{Ga + In} \quad (11)$$

where  $Ga$  is the mole fraction of gallium and  $In$  is the mole fraction of indium. The bandgap  $E_g$  ranges from 1.01 V to 1.64 V as the Ga mole fraction is increased from zero to one following [16]

$$E_g = 1.010 + 0.626x - 0.167x(1-x). \quad (12)$$

Traditionally, with silicon solar cells, a homojunction is formed at the border between the  $n$ -type and  $p$ -type portions of the semiconductor. Cu(InGa)Se<sub>2</sub> solar cell do not form a homojunction but rather a heterojunction as a result of the differences in electrical properties between the materials. Specifically, due to the differences in

bandgaps of the two materials that form a junction, discontinuities in the band diagrams occur which may create barriers to the flow of carriers [16].

### 1. n-CdS/Cu(InGa)Se<sub>2</sub> Solar Cell Design

Much like other solar cells, the standard Cu(InGa)Se<sub>2</sub> cell follows traditional structure designs containing a top contact, a window layer, a buffer layer, an absorber layer, a back contact layer, and the substrate in which it is placed. The standard structural layout of a Cu(InGa)Se<sub>2</sub> cell is illustrated in Figure 8. Additionally, a cutline from the top of the cell to the bottom provides a band-structure diagram as demonstrated in Figure 9.

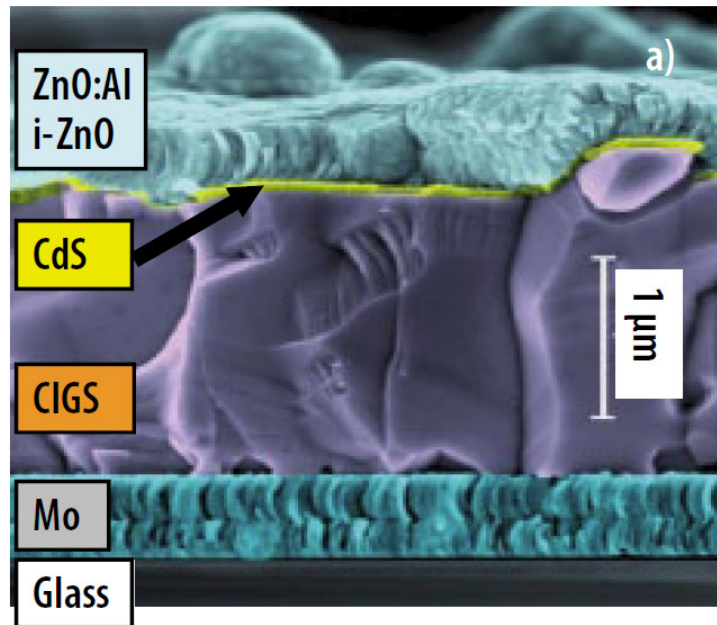


Figure 8. Colorized scanning electron microscope image of Cu(InGa)Se<sub>2</sub> structure, from [19].

There are several substrate options for the Cu(InGa)Se<sub>2</sub> solar cells, with the most popular options being soda lime glass and thin metal films. Soda lime glass is a rigid structure but has been used in most of the research due to the simplicity and stability of its application as well as its low cost. Thin film metal substrates are used less often but have the largest upside future for commercial production. The thin film metal substrate is

both lighter and more flexible than the soda lime glass but come with a higher relative cost.

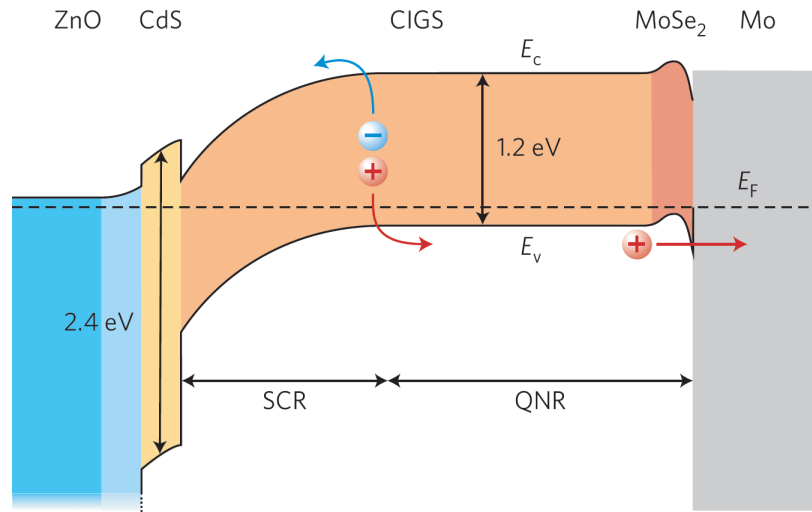


Figure 9. Band structure for Cu(InGa)Se<sub>2</sub> solar cell, from [20].

The next layer above the substrate in the cell is the molybdenum (Mo) back. This layer serves to not only as the bottom contact but also as part of the substrate. Several materials have been investigated, but Mo has been shown to be the best choice as it demonstrates low electrical resistance, is resistive to Cu and In permeation, and is stable at temperatures required for processing [21].

The third layer is the *p*-type Cu(InGa)Se<sub>2</sub> absorber. The primary difference observed between absorber layers in different designs is the Ga concentration as a result of the tunable bandgap. Furthermore, the thickness of the absorber layer varies significantly between cells. While it is important to keep the absorber layer thin to maintain the cell's flexibility, it is a widely studied parameter. Ultra-thin CIGS absorber layers have been studied and efficiencies have been simulated to be in the 10–11% range but have not been widely produced [22]. Thicker layers have also been studied, but thicknesses is typically limited to about 3.0  $\mu\text{m}$  to keep the overall size of the cell small, maintain its flexibility, and ensure that the cell does not become too wide to harvest the available carriers before recombination occurs.

Typically, an *n*-type cadmium sulfide (CdS) thin film is used as a fourth buffer layer. This buffer layer serves as the *n* portion of the *p-n* junction and typically has a thickness of 0.05-0.1  $\mu\text{m}$  [16]. CdS is a good choice for this buffer layer because it has a bandgap of 2.4 eV, which allows a majority of photons to pass through to the Cu(InGa)Se<sub>2</sub> absorber layer [19]. Only photons with a wavelength shorter than 500.0 nm can be absorbed by the CdS layer. While most Cu(InGa)Se<sub>2</sub> solar cells produced use the CdS, it is undesirable due to the fact that it falls into the category of heavy metals and creates concerns for both the environment and anyone who comes into contact with it. Furthermore, the use of a CdS buffer layer requires a thin intrinsic ZnO layer to be deposited between the buffer layer and the transparent conducting oxide layer which adds an additional step to the manufacturing process.

The top layer is a ZnO window layer. It consists of a very thin intrinsic ZnO layer topped with an aluminum (Al) doped ZnO transparent conducting oxide layer. This layer serves to allow for photons to pass through while simultaneously allowing for the conduction of current generated by the cell [16].

The top contact is placed on top of the window layer and is typically made of a grid of Al. This is necessary to allow for the collection of carriers generated within the solar cell.

## **2. Developments in Cu(InGa)Se<sub>2</sub> Design**

Several studies have been published aimed at comparing buffer layers to determine if a viable alternative to CdS exists. The most promising is the use of an *n*-type ZnO buffer layer in place of the traditional CdS. ZnO has a bandgap of 2.8 eV, which increases the wavelength spectrum that passes through the buffer layer into the absorber layer [19]. Despite the promise of ZnO buffer layers, many studies demonstrated that using ZnO in place of CdS results in a cell with a 3–5% lower efficiency [16]. Regardless, some companies and researchers continued exploring the use of ZnO as an alternative to CdS. Recently, record setting cells with efficiencies nearing 21% were fabricated using the ZnO buffer layer, proving that ZnO remains a viable replacement for CdS as the buffer layer in a CIGS cell [23].

Another advancement in the design of Cu(InGa)Se<sub>2</sub> cells is the inclusion of graded Ga concentration within the absorber layer in order to increase the overall efficiency of the solar cell. The first method is known as back grading, where the concentration of Ga is increased moving towards the back contact. The second method is known as front grading, where the Ga concentration is decreased moving towards the back contact. The third is essentially a blend of the first two concepts, in which higher Ga concentration at both the top and bottom contacts is achieved with a minimum Ga concentration in the middle of the absorber layer [24].

### C. TRAP DENSITY IN CIGS ALLOYS

One of the primary concerns in the design of Cu(InGa)Se<sub>2</sub> solar cells is the determination of the Ga concentration to be used. Given the tunable bandgap that Cu(InGa)Se<sub>2</sub> possesses, it was initially thought that a higher Ga concentration, which leads to a higher bandgap, would result in a cell with a higher efficiency. Through experimentation, it was found that this was not the case; an ideal Ga concentration of around 0.3 mole fraction has been found to result in the highest efficiency cells [16]. This phenomenon required investigation as to why the efficiency did not follow the expected increase predicted by theory.

Recently, a study published measured the trap density within Cu(InGa)Se<sub>2</sub>. It was found that trap density is a function of Ga concentration [25]. The relationship between trap density and bandgap, which is directly proportional to mole fraction, is illustrated in Figure 10. The result is that the increases in efficiency that are expected from a higher Ga concentration are offset by the higher trap density associated with that higher Ga concentration, supporting the idea that cells with Ga mole fractions around 0.3 achieve the highest efficiencies [25]. Furthermore, this plot includes data from an analysis of devices produced by both the single-stage process as well as the three-stage process. The conclusion is that the three-step process results in a better overall structure with fewer defects [25].

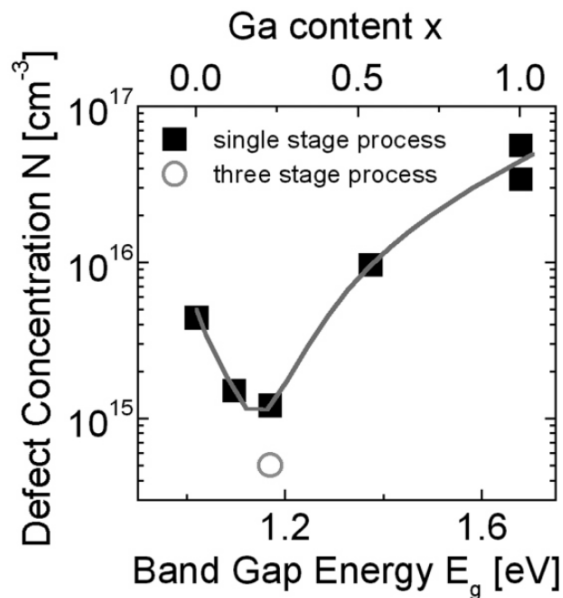


Figure 10. Plot of defect concentration versus Ga composition, from [25].

The study from which Figure 10 originated was limited to a single data point for the three-stage process, which does not provide a sufficient basis for this trap density to be used. Further studies of the density of traps have resulted in a wide range of reported values for the trap density in  $\text{Cu}(\text{InGa})\text{Se}_2$  produced using the three-stage process. Most trap densities are reported with a magnitude of  $10^{14}$ ; a more realistic profile was created based on these results as illustrated in Figure 11. [26] The minimum trap density reported is  $1.2 \times 10^{14}$  for a mole fraction of 0.24. Results have been reported for trap densities measured an order of magnitude or more [26], [27] less than the results in Figure 10. The profile of average reported trap densities for  $\text{Cu}(\text{InGa})\text{Se}_2$  produced using the three-stage process is illustrated in Figure 11.

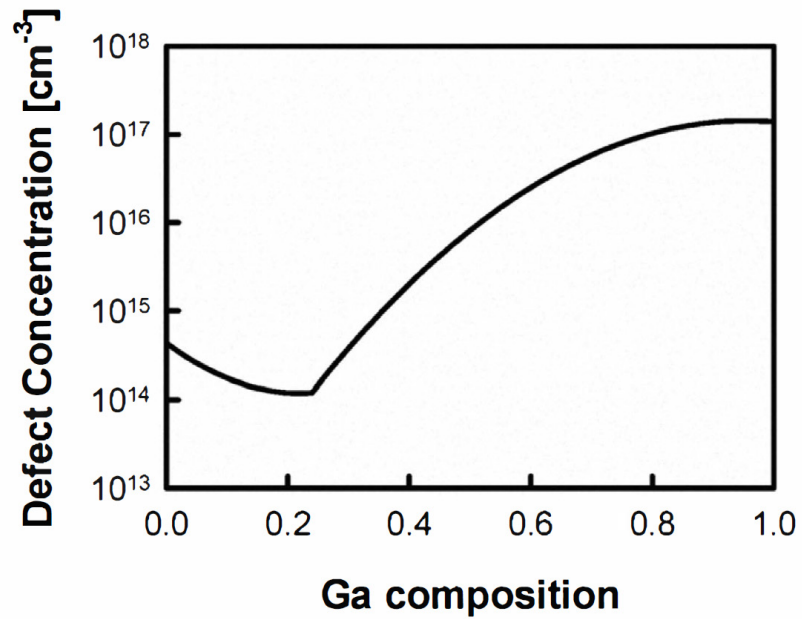


Figure 11. Average defect concentration as a function of Ga composition, from [26].

THIS PAGE INTENTIONALLY LEFT BLANK

### III. TCAD MODELING OF Cu(InGa)Se<sub>2</sub> CELLS

#### A. SILVACO ATLAS INTRODUCTION

SILVACO is a software package that allows for the modeling and simulation of many semiconductor devices. Within SILVACO, there are many subprograms including ATLAS and TONYPLOT. ATLAS is a program that allows the user to create a semiconductor and perform analysis and simulations through a series of input and output statements. TONYPLOT allows the user to display the information generated within the ATLAS submodule in a useful manner [28]. For example, ATLAS has the ability to create and simulate solar cells and using the data from these simulations, the user can create the IV curve using TONYPLOT.

The simulations performed for this thesis were completed by accessing ATLAS using Deckbuild. Deckbuild is a user interface that allows for the set of input statements to be arranged beginning with a designation to perform the actions inside of the ATLAS program. Using ATLAS, the user is given the ability to define any desired characteristics of a semiconductor device including material, dimensions, physical and electrical properties, and many other pertinent quantities. ATLAS also has a built in library for many common materials, and if the user does not specify a particular variable, it is pulled from that library [28].

Particularly for the purposes of this thesis, ATLAS contains statements that allow for the specification of composition gradients as well as trap densities. The ability to specify composition gradients allows for the simulation of a CIGS solar cell that contains unique concentration gradients within the absorber layer. The inclusion of finite trap densities is a key factor to properly simulate a CIGS solar cell [28]. As discussed in Chapter II, trap density varies with Ga composition in the absorber layer of CIGS cells. Specifying trap density based on experimental data creates a more accurate simulation than relying on the constant trap density value contained in ATLAS' built in library.

Once the user has specified the inputs, ATLAS conducts a physics-based simulation of the created device [28]. For solar devices, this includes creating the device

itself as well as recording its behavior as it is exposed to a designated solar spectrum. For the purposes of this analysis, AM1.5 was used and is resident inside of the standard ATLAS library; this information contains the wavelength and power specifications for this particular solar spectrum and uses these established values for the simulation. ATLAS also takes into account the appropriate reflection and refraction properties of the materials present in a solar cell in order to ensure a realistic propagation of the illumination through the cell.

## **B. ATLAS FUNCTION**

In order for ATLAS to complete the physical based simulation of the input files, it solves several sets of equations based on a mesh established by the user. The mesh statement within ATLAS creates a two dimensional set of nodes that are used for the numerical solving and simulation of devices. A larger number of nodes results in a more accurate simulation of the device but a longer simulation run time. To combat this, the user can specify different node intervals for different portions of a device, allowing the user to optimize the mesh to generate convergent solutions in the minimum time necessary.

Through an analysis of a particular device, the areas that require a higher density of nodes can be determined. Any sharp corners, such as near a contact or channel, require a larger number of nodes to ensure that the simulation converges and accurately simulates the behavior of the device. Junctions also require a higher density of nodes; for example, at a  $p-n$  junction, a depletion region occurs. In order to properly model and simulate this depletion region, a higher density of nodes is required. If a large portion of bulk exists, a lower density of nodes can be used since there is less variation in behavior within that portion of the device. A sample of the meshing apparent in a solar cell is illustrated in Figure 12.

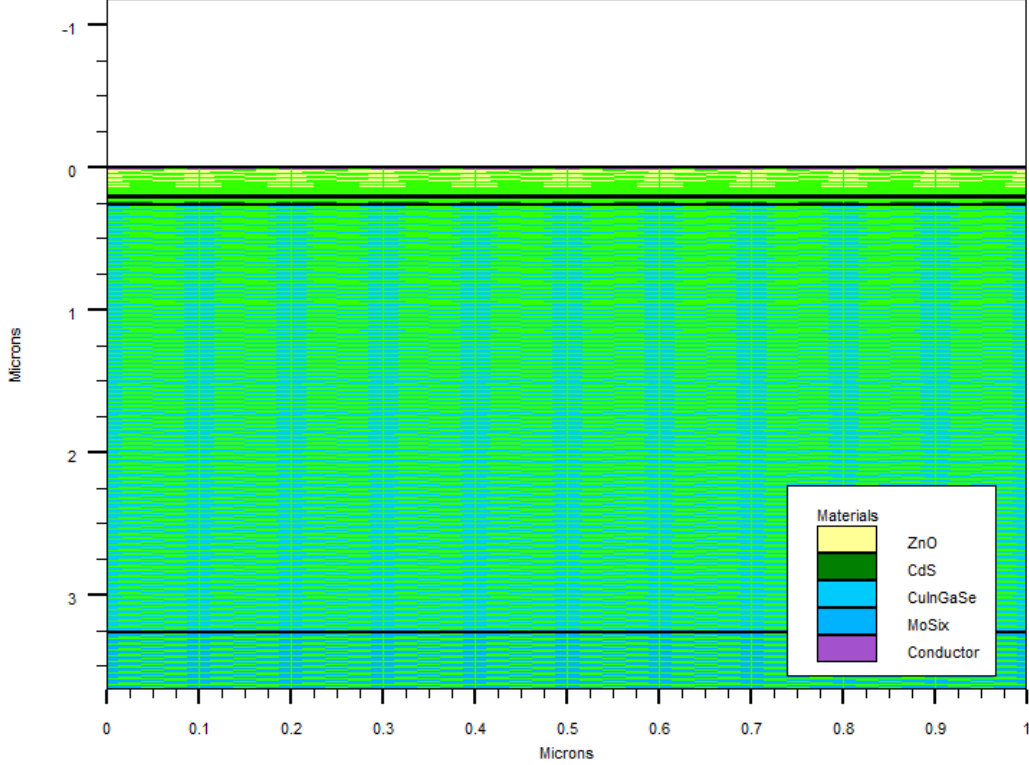


Figure 12. Basic Cu(InGa)Se<sub>2</sub> cell structure file showing mesh.

The equations which are solved in ATLAS, pertinent to the simulation of solar cells, can be broken down into Poisson's equation, transport equations, and continuity equations.

### 1. Poisson's Equation

The first equation considered is Poisson's equation. Poisson's equation is what ATLAS uses to calculate the relationship of space charge density to electrostatic potential [28]. Poisson's equation is

$$\nabla^2 V = -\frac{\rho}{\epsilon} \quad (13)$$

where  $\nabla$  is the gradient operation,  $\epsilon$  is the permittivity, and  $\rho$  is free charge density.

## 2. Transport Equations

ATLAS uses the drift-diffusion transport model to simulate the movement of carriers within a created device. This transport model is calculated based on drift and diffusion currents within a given material. The electron current density is [28]

$$J_n = qn\mu_n E + qD_n \nabla n \quad (14)$$

where  $q$  is charge of an electron,  $n$  is the electron density,  $E$  is the electric field,  $\mu_n$  is the electron mobility, and  $D_n$  is the electron diffusion constant. The first term in Equation (14) accounts for the drift of electrons, while the second term accounts for the diffusion of electrons. The hole current density is [28]

$$J_p = qp\mu_p E - qD_p \nabla p \quad (15)$$

where  $p$  is the hole density,  $\mu_p$  is the hole mobility, and  $D_p$  is the hole diffusion constant. The first term in Equation (15) accounts for the drift of holes, while the second term accounts for the diffusion of holes.

## 3. Continuity Equations

The continuity equations used by ATLAS are implemented to keep track of carrier changes throughout the simulation process. The electron continuity equation is [28]

$$\frac{\partial n}{\partial t} = \frac{1}{q} \text{div} \vec{J}_n + G_n - R_n \quad (16)$$

where  $\vec{J}_n$  is electron current density,  $G_n$  is the electron generation rate, and  $R_n$  is the electron recombination rate. Similarly, the hole continuity equation is [28]

$$\frac{\partial p}{\partial t} = -\frac{1}{q} \text{div} \vec{J}_p + G_p - R_p. \quad (17)$$

where  $\vec{J}_p$  is hole current density,  $G_p$  is the hole generation rate, and  $R_p$  is the hole recombination rate.

## C. ATLAS OUTPUT

Within the input file, the user has the ability to specify the outputs desired from the simulation. Standard outputs include a log file from the simulation, a structure file

from the simulation, and the output of desired parameters. The log file output allows for the creation of graphs of the data collected during the simulation, including quantum efficiencies and IV curves. The structure files provide the information for a detailed analysis of the device such as examining the internal electric fields and photogeneration rates. Combined with specifying the output of appropriate variables, the user can create a band diagram of the structure.

#### **D. INITIAL MODEL DEVELOPMENT**

With an understanding of ATLAS' function and how it simulates a device using physical modeling, development of the model to be used in simulations can begin. The construction of the model began with a basic cell to verify the proper implementation into ATLAS and the ability to produce results. The model is created as a 1.0  $\mu\text{m}$  by 1.0  $\mu\text{m}$  cell; the small cell facilitates a manageable simulation time while still being large enough to simulate pertinent physical and electrical properties and interactions that are expected in a larger cell. Once the simulation is complete, pertinent quantities can be extracted and calculated.

The initial model solar cell consisted of a Mo layer 0.4  $\mu\text{m}$  thick, a Cu(InGa)Se<sub>2</sub> absorber layer 3.0  $\mu\text{m}$  thick with a 0.3 Ga mole fraction, a CdS buffer layer 0.05  $\mu\text{m}$  thick, a 0.01  $\mu\text{m}$  intrinsic ZnO layer, and a window layer 0.2  $\mu\text{m}$  thick. These values were based on a combination of work done by previous NPS students and data that had been measured and reported [9], [10], [22]. Trap density is determined using the specified mole fraction in conjunction with extrapolation from Figure 11. For additional material parameters in the model, the simulation relied on the values that are resident in the ATLAS library for the materials used in the cell.

The model was illuminated with the AM1.5 spectrum to simulate the spectrum observed by terrestrial cells as well as produce results comparable to other published research results. Furthermore, the cell was simulated at 25 C in order to be able to be compared to other published results.

THIS PAGE INTENTIONALLY LEFT BLANK

## IV. SIMULATION AND RESULTS

### A. SINGLE ABSORBER LAYER

Simulations began with the basic cell described in Chapter III to verify the proper implementation in ATLAS and the ability to produce results. This cell functioned properly and was able to produce results consistent with those published for CIGS solar cells; the cell's efficiency was simulated at 17.34%. The cell structure is illustrated in Figure 13.

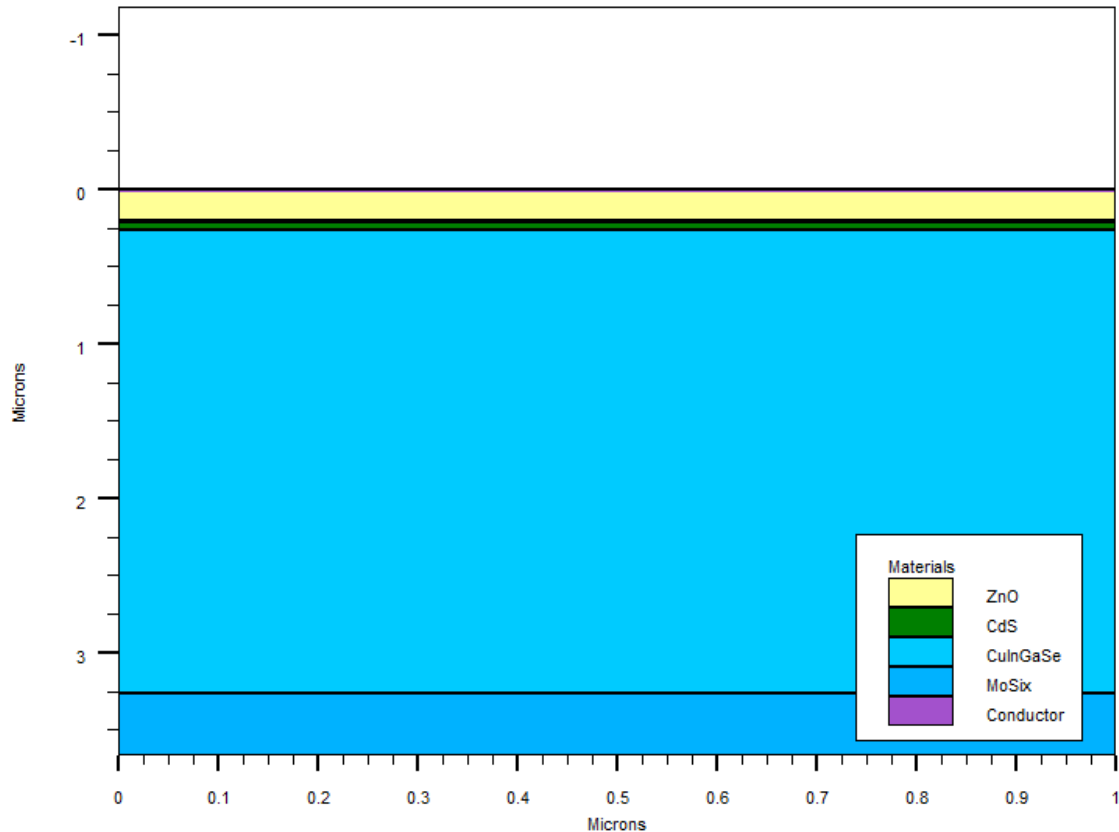


Figure 13. Structure output showing electric-field strength for baseline cell.

After verification of the basic cell, the first change was from an absorber layer with constant Ga concentration to one with a graded concentration. The first attempts only had a single gradient in the absorber layer, which was varied for a variety of slopes,

all with a midpoint Ga mole fraction of 0.3. The slope value is the overall Ga mole fraction change from the top of the absorber layer to the bottom. A positive slope corresponds with a decreasing Ga concentration moving from the top of the cell to the bottom, while a positive slope corresponds to an increase in Ga concentration moving from the top of the cell to the bottom. The IV curves resulting from these simulations are shown in Figure 14.

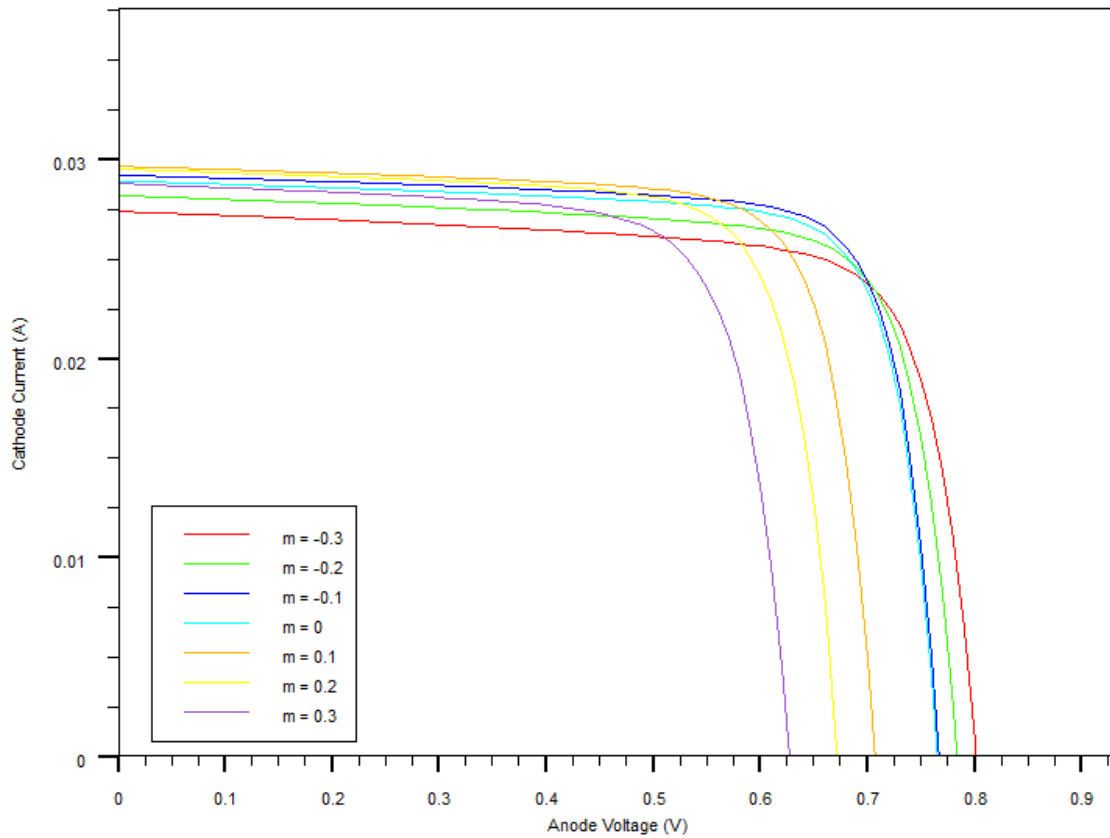


Figure 14. Family of IV curves for single-graded absorber layer simulations.

To more clearly illustrate the effect of the graded absorber layer, efficiency as a function of slope is illustrated in Figure 15. The maximum efficiency recorded was for the cell with the smallest forward graded absorber, with a slope of  $-0.1$ , resulting in an efficiency of 17.42%. This is most likely due to the increased internal electric field stemming from the concentration gradient in the absorber. Furthermore, it was observed that for positive slopes open circuit voltage increased whereas negative slopes resulted in

a decrease in open circuit voltages for the cells. This effect can be contributed to an opening of the bandgap near the  $p$ - $n$  heterojunction which helps align the valence and conduction bands.

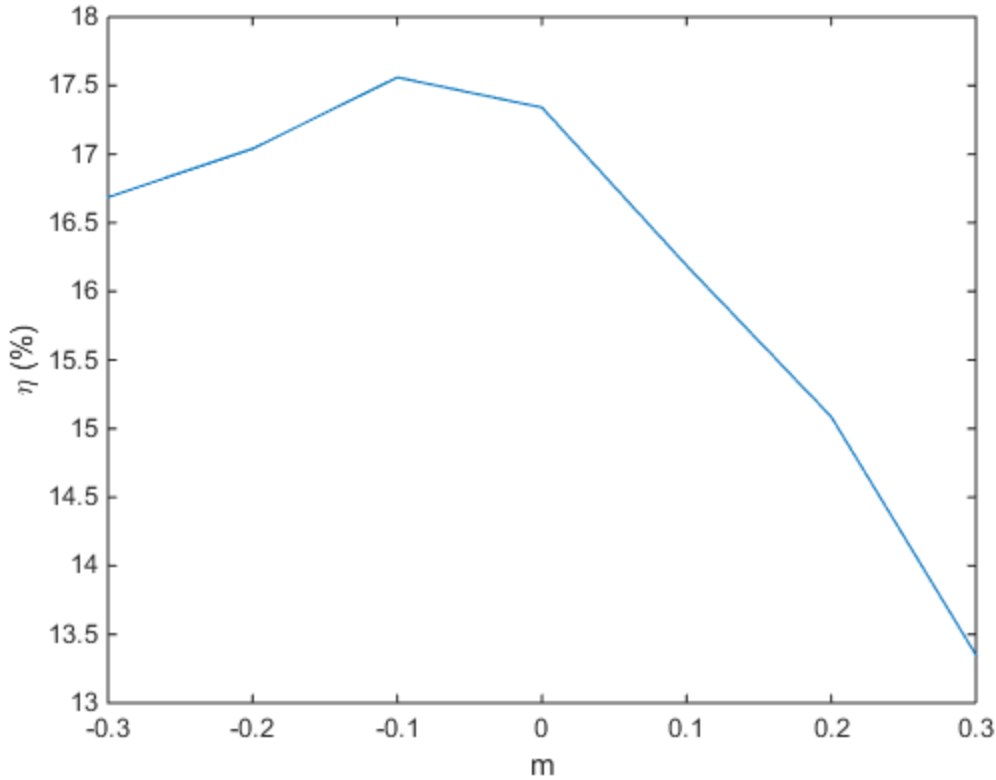


Figure 15. Single-absorber layer efficiencies plotted as a function of slope.

## B. DUAL-GRADED ABSORBER LAYER

The second simulated cell was modeled with an absorber layer divided into two equal sections that allow for the specification of two Ga concentration gradients. Creating a decreasing gradient from top to bottom in the top absorber layer creates a front field that sweeps photo-generated carriers towards the  $p$ - $n$  heterojunction. The creation of an increasing gradient from top to bottom in the bottom absorber layer creates a back field that sweeps photo-generated carriers towards the back contact. The combination of these two fields should increase the overall efficiency of the cell by sweeping carriers towards the contacts before they can recombine, as discussed in Chapter II. Using the structure files produced from ATLAS, we can compare the electric fields within the absorber layer

from a device with an ungraded absorber layer to the structure file of the device with dual-concentration gradients. An example profile for the concentration gradient used is illustrated in Figure 16.

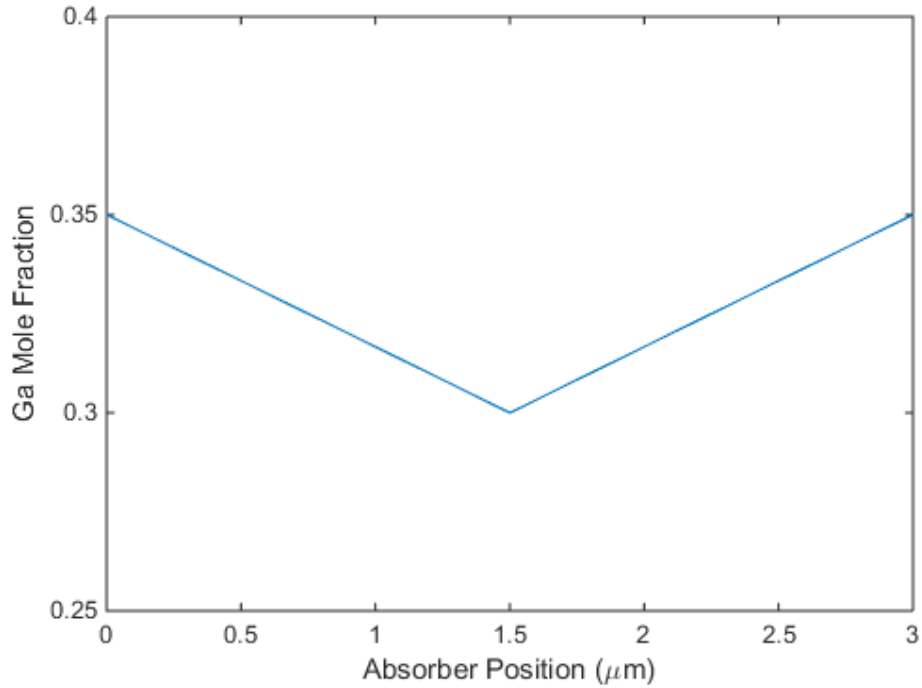


Figure 16. Example mole fraction profile for a dual-graded absorber layer.

As with the single-absorber layer simulations, a range of slopes were chosen in order to determine the slope that maximizes the output of the cell. After observing the severe drop off in efficiency and the decrease in open circuit voltage for positive slopes in the single absorber cell, fewer data points were simulated for positive slopes. In addition, more slope values were used for the negative slopes, where the highest efficiencies were observed, in order to provide better resolution in the results. For each simulation, the slope of both the front and back gradients were set to the same value, and the results of these simulations are illustrated in Figure 17.

The largest efficiency of 17.42% was observed for the cell with the smallest negative slope. This slope corresponds to the top absorber layer having concentration decreasing from a Ga mole fraction of 0.35 to 0.3 going from the top of the layer to the

bottom. For the bottom layer, the Ga mole fraction was increased from 0.3 to 0.35 going from the top to bottom.

Much like the single-absorber layer simulations, the higher magnitude negative slopes resulted in increases in the open circuit voltage. The short circuit currents decreased significantly for these higher slopes, resulting in an overall decrease in efficiency. The increased trap density stemming from the increase in Ga concentration in these devices caused this decrease in short circuit current. Fill factor was also reduced for these models, where trap density has a significant impact on the short circuit current as it also decreases the maximum power current.

These results are consistent with the predicted electric fields that result from having dual-graded absorber layers. The electric field present in a cell without a graded absorber layer is illustrated in Figure 18.

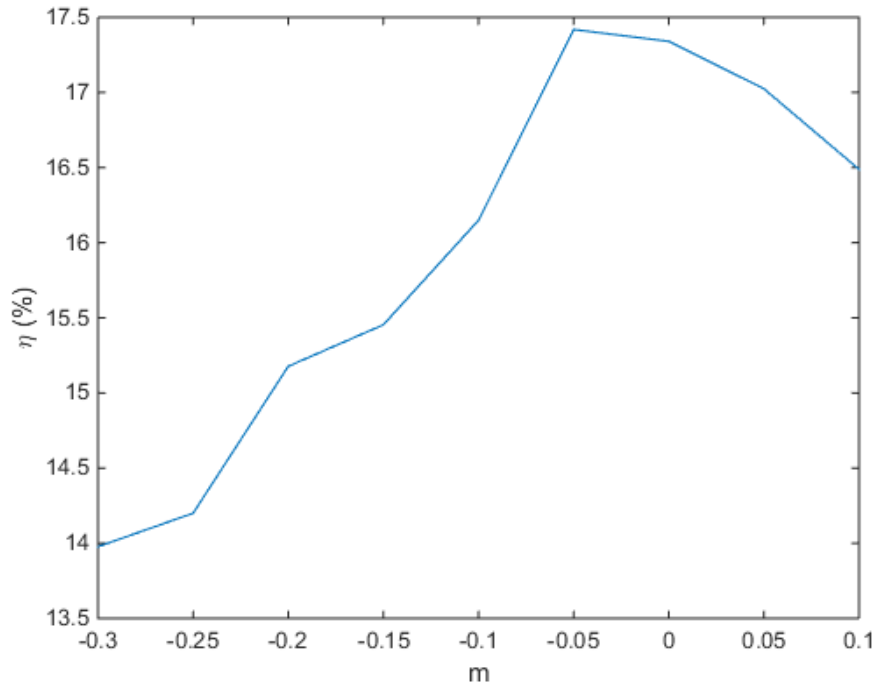


Figure 17. Dual-absorber layer efficiencies plotted as a function of slope.

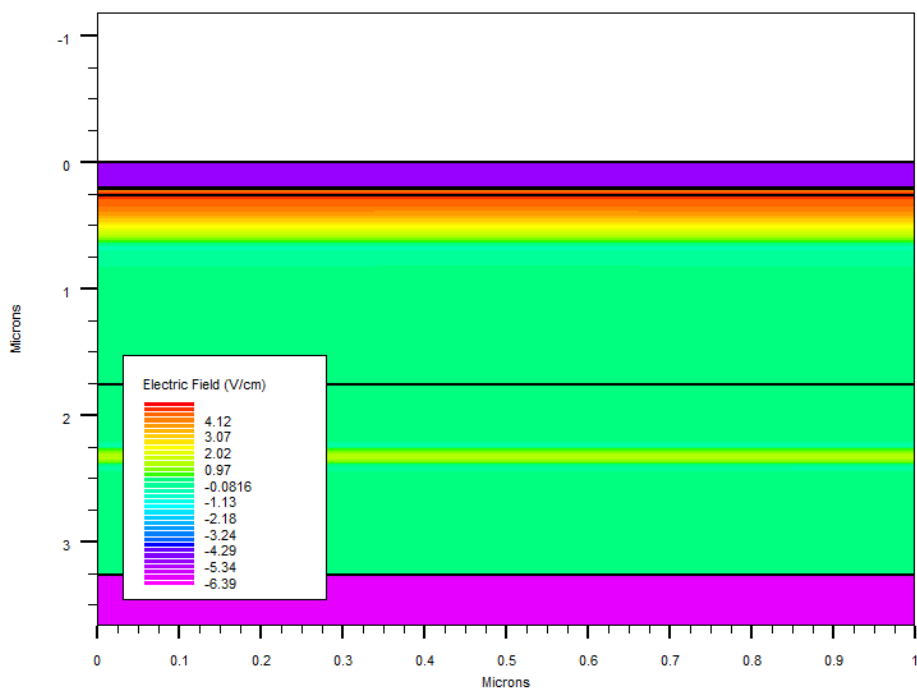


Figure 18. Structure output showing electric-field strength for an ungraded absorber.

For comparison, the electric field for the cell that produced the highest efficiency with graded absorber layer is illustrated in Figure 19. The legends for the colors associated with the electric fields are the same in the two figures, allowing for a comparison of the relative strengths. The electric field is clearly stronger in the cell with a graded absorber layer than the cell with constant Ga concentration.

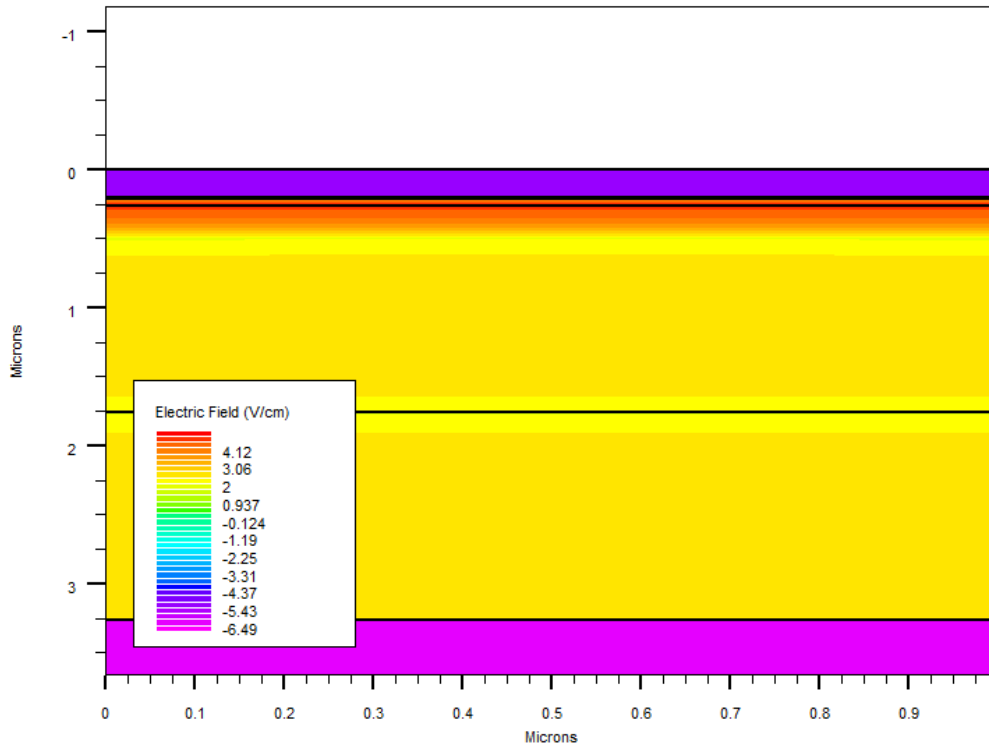


Figure 19. Structure output showing electric-field strength for a graded absorber.

### C. TRAPEZOIDAL ABSORBER LAYER

The gradients are important, but in the manufacturing process of creating these gradients, the profile tends to assume a profile similar to the concentration profile discussed in Chapter II. This was accomplished by the addition of a third layer within the absorber. This allowed for a constant Ga concentration in the middle of the overall absorber layer that, in combination with the front and back gradients, create a more accurate trapezoidal model. An example profile for the concentration gradient used is illustrated in Figure 20. The resulting structure of this file is illustrated in Figure 21. Building on the work done with the dual-graded absorber layer, the same range of slope values were simulated for this trapezoidal model. The results of these simulations were similar to those for the dual-graded absorber layer with the smallest negative sloped cell achieving the highest efficiency at 17.38%, as illustrated in Figure 22. Although this is a drop in efficiency from the dual-graded absorber layer, its overall realistic design makes it a better choice for implementation in future models.

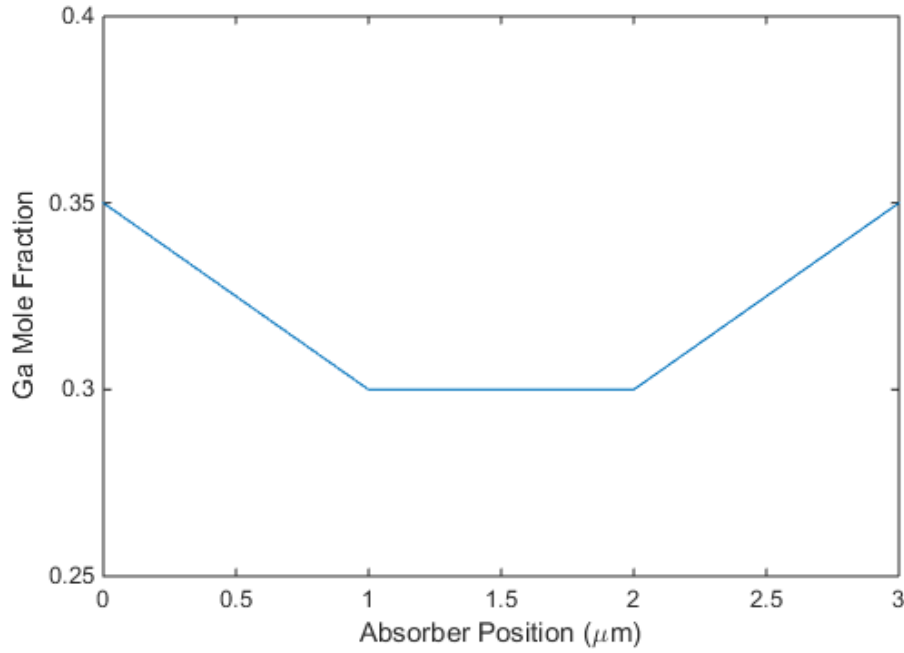


Figure 20. Example mole fraction profile for a trapezoidal absorber layer.

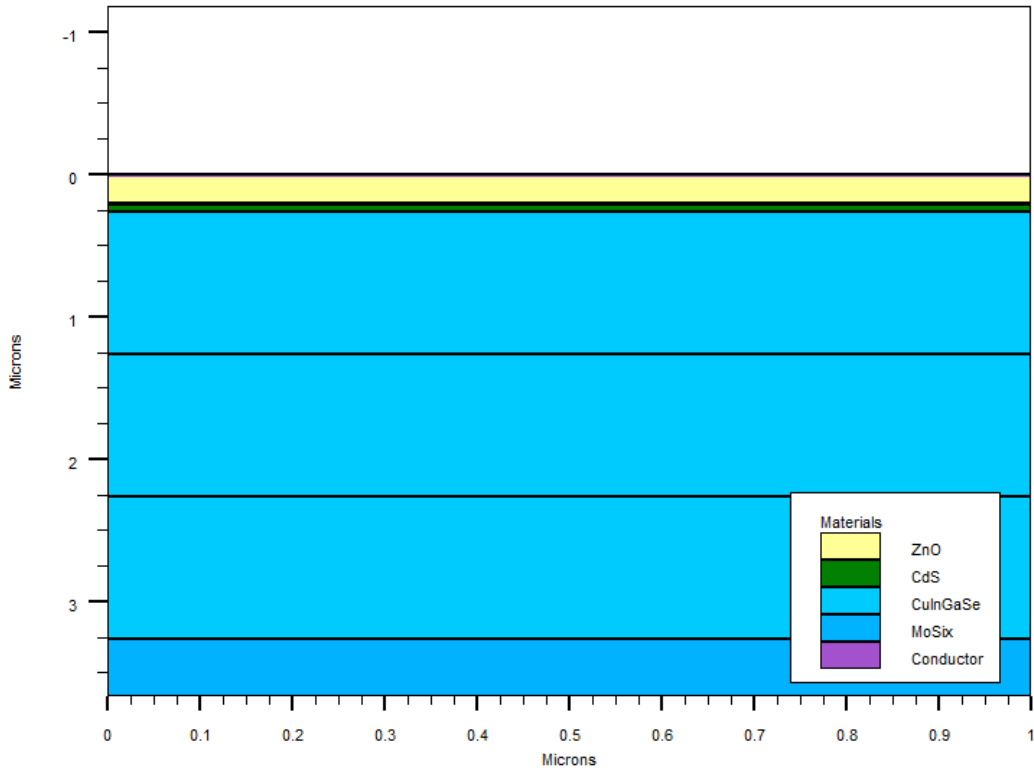


Figure 21. Structure output showing electric-field strength for trapezoidal-graded absorber.

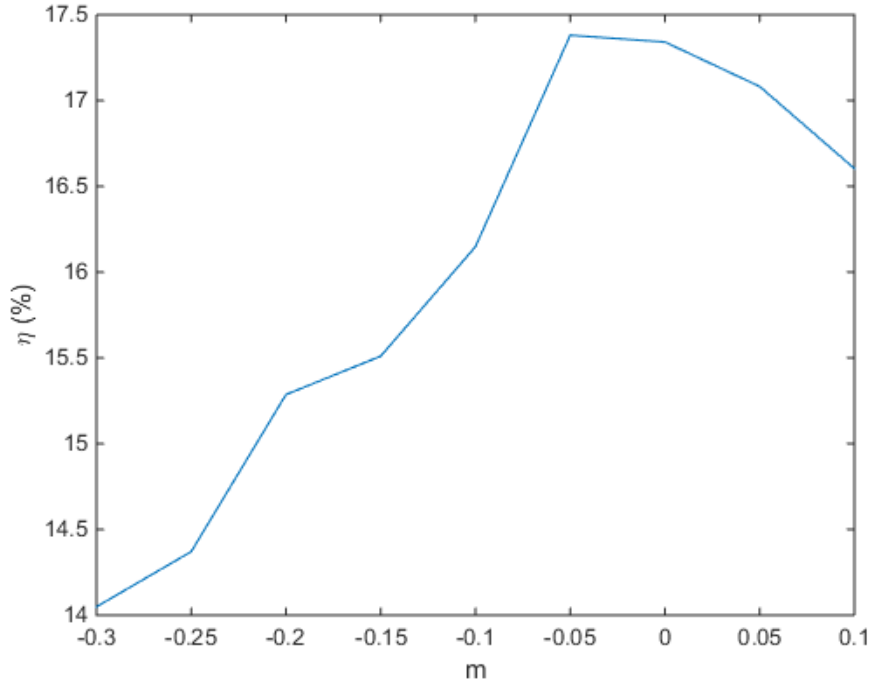


Figure 22. Trapezoidal absorber layer efficiencies plotted as a function of slope.

As with the dual-graded absorber layer results, a decrease in short circuit current and an increase in open circuit voltage were observed with larger negative values of  $m$ . This further emphasizes the impact of trap density as a significant factor in the modeling of Cu(InGa)Se<sub>2</sub> cells. Furthermore, for most slope values, an increase in efficiency was observed for the trapezoidal shaped absorber layer. This result supports what was found in literature and discussed in Chapter II.

#### D. ALTERNATE BUFFER LAYER

Having demonstrated the ability to integrate an absorber layer with dual-concentration gradients, the next step was to replace the CdS buffer layer with ZnO buffer layer. As discussed in Chapter II, the ZnO buffer layer typically decreases the output of cells produced in the laboratory. Following the successful implementation of a ZnO buffer layer by Solar Frontier, resulting in a record breaking 20.9% efficiency, we found that it has been experimentally proven as a viable alternative to CdS [22]. The use of the ZnO buffer layer in place of the CdS layer reduces the hazardous materials used in the device, and the simulations determine if degradation in device performance results. In

addition, it reduces the number of required manufacturing steps through the elimination of the intrinsic ZnO layer required for CdS.

Keeping all other variables constant from the previous model that used the trapezoidal-graded absorber layer, a file was created using a ZnO buffer layer; the thickness from the CdS buffer layer was used for the initial simulation. The resulting model achieved an efficiency of 22.97%. The increase in efficiency of the cell was more than expected and required further study to understand what contributes to such an increase. Using data extracted in ATLAS, we observed and analyzed the band diagrams in order to provide some of this information. Of primary concern is the  $p-n$  heterojunction differences with the two buffer layers. The band diagram for the cell with the CdS buffer layer is illustrated in Figure 23.

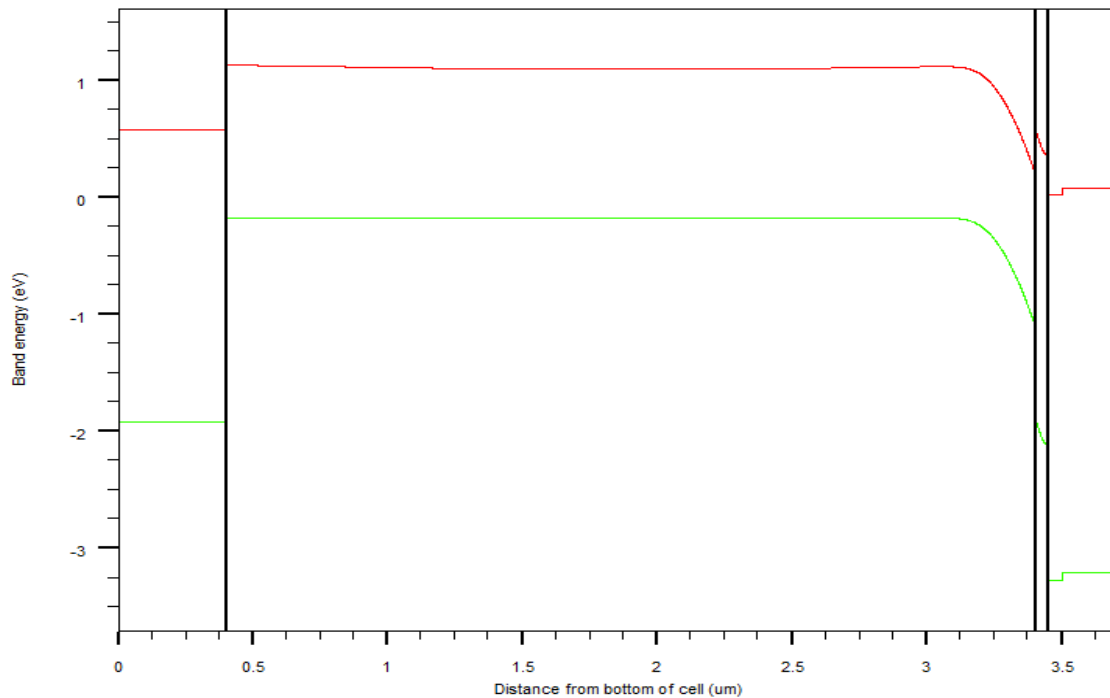


Figure 23. Band diagram for a cell with a CdS buffer layer.

The band diagram for the cell with the CdS buffer has an abrupt increase in the conduction band energy level where the  $\text{Cu(InGa)Se}_2$  absorber layer meets the CdS buffer layer. This increase in conduction band energy serves to create a barrier that

inhibits the drift current of electrons in the cell. The band diagram for the cell with the ZnO buffer layer is illustrated in Figure 24. The barrier observed in the conduction band is no longer present in the band diagram for the ZnO buffer layer.

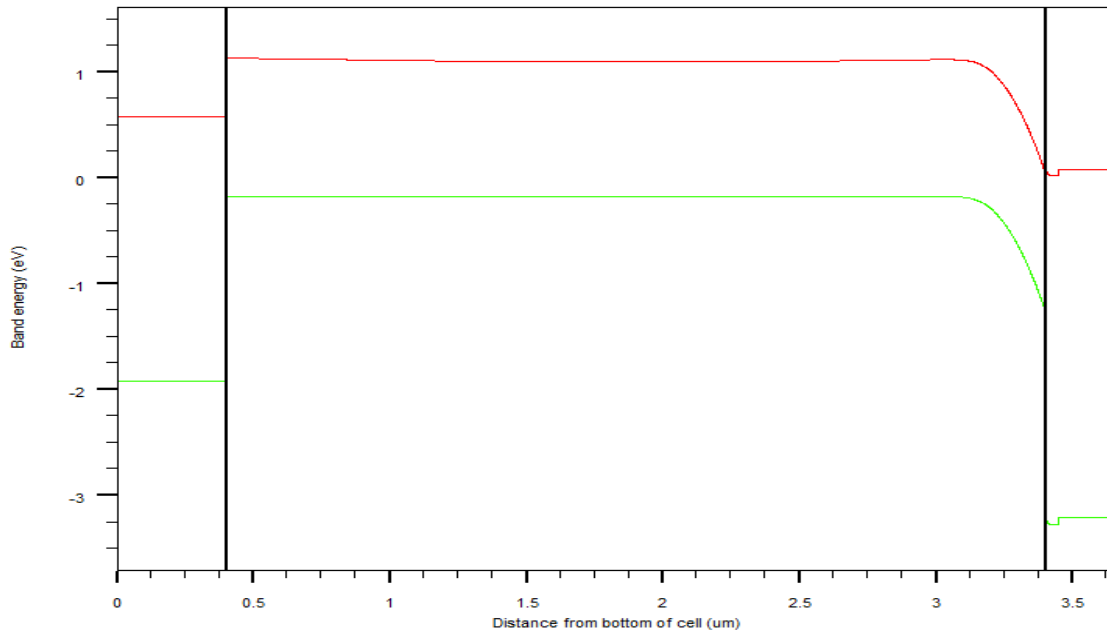


Figure 24. Band diagram for a cell with a ZnO buffer layer.

With an understanding of the band diagrams to explain the increase in performance, an analysis of buffer layer thickness can be completed. The thickness was varied, and this analysis found that a thickness of 10.0 nm provided the optimum efficiency of the cell, achieving 23.01%. The results of this analysis are shown in Figure 25.

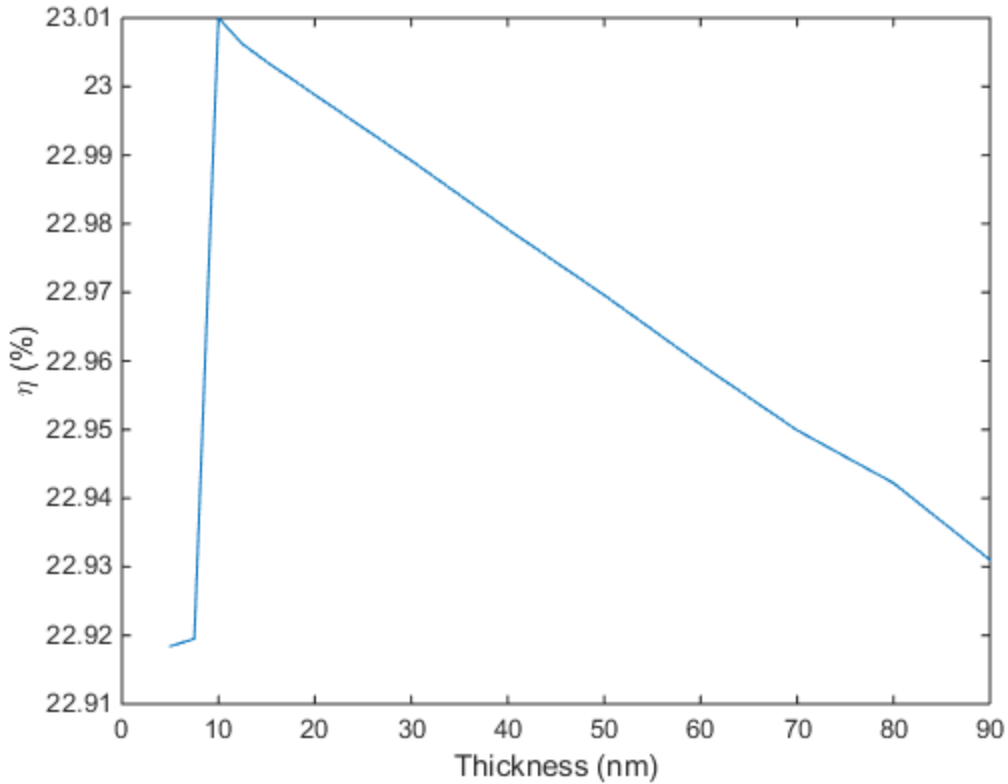


Figure 25. ZnO buffer layer efficiencies plotted as a function of thickness.

### E. TOP GRID

The final step in optimizing the model was to include a top grid on the device. Cu(InGa)Se<sub>2</sub> cells are typically topped with a grid of aluminum; the inclusion of this top grid allows for a more accurate simulation that includes the impact of top shading. To integrate this top grid, a single strip of aluminum with sufficient thickness to create shading within the absorber layer was included. The strip of aluminum is 0.1  $\mu\text{m}$  thick, which is 10% of the top surface area of the cell. This step proved to be one of the most challenging as it required a significant revision of the mesh for the cell to ensure that the simulation converged as well as providing accurate results. The addition of the grid required the addition of a vacuum on both sides to allow the light beam to reach the cell. It also created sharp corners in the  $x$ -direction that previously did not exist, requiring a much denser mesh around these areas.

The effect of the top grid is illustrated in Figure 26 and Figure 27. These figures show a decrease in the photogeneration rate below the top contact. This is a result of the aluminum contact reflecting light rather than allowing it to pass through like the ZnO window layer typically does. The result of the reduced photogeneration rate is a reduction in the photogenerated current, which decreases the output of the cell. The cell with the addition of the top grid achieved an output of 21.14%. Compared to the cell without a grid, the output was reduced by 1.87%, which follows the expected output reduction discussed in Chapter II.

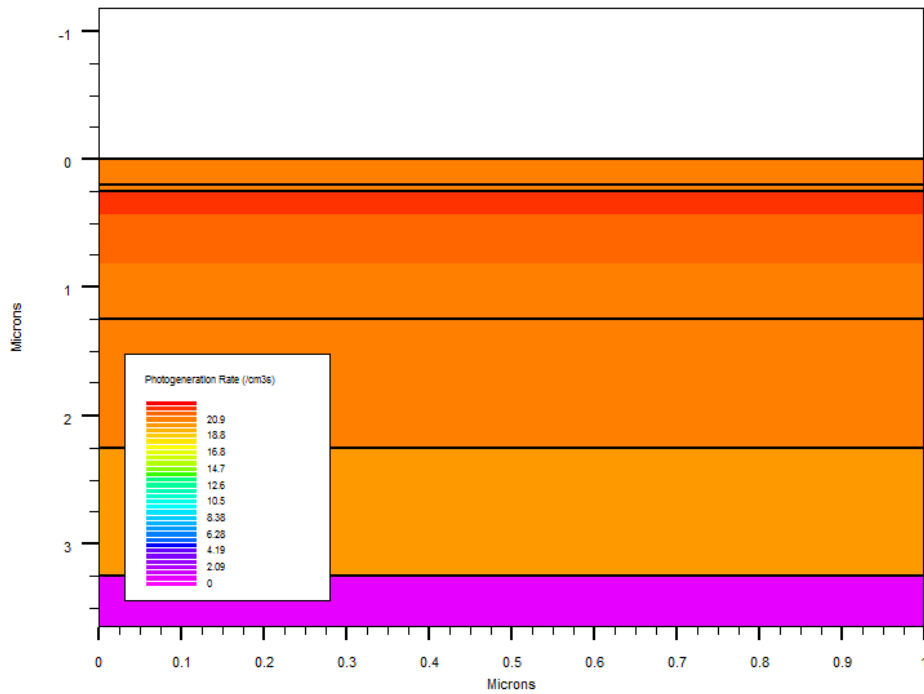


Figure 26. Photogeneration plot for a cell without a top contact grid.

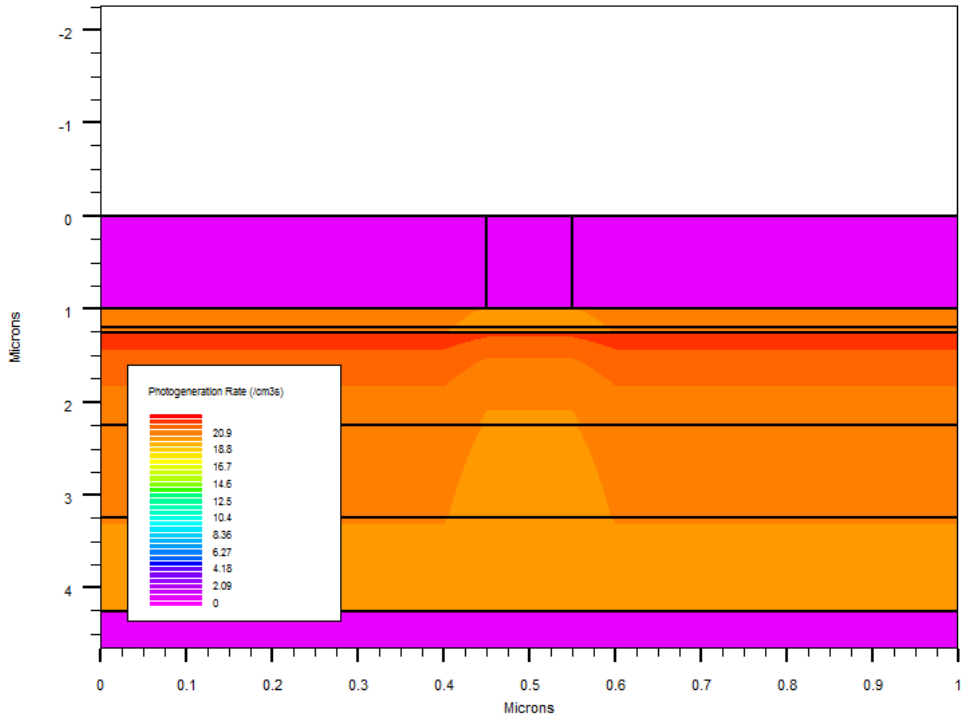


Figure 27. Photogeneration plot for a cell with a top contact grid.

## V. CONCLUSIONS AND RECOMMENDATIONS

### A. CONCLUSIONS

The objective of this thesis was to simulate a new Cu(InGa)Se<sub>2</sub> solar cell design that implemented a graded absorber and a non Cd based buffer layer. Through the use of SILVACO's ATLAS simulation software, a model was created and revised in a stepwise fashion to create and simulate designs to achieve this objective. Modeling began with the confirmation of a simple model of a Cu(InGa)Se<sub>2</sub> solar cell which achieved an efficiency of 17.34%. From this model, the absorber layer was graded, and the optimum gradient was found to begin with a mole fraction of 0.35 at the top and end with a mole fraction of 0.25 at the bottom. The absorber layer was then broken into two sublayers to allow for the creation of both front and back graded portions. This proved a successful implementation of the dual-graded absorber layers, with a top efficiency of 17.42% being achieved. The simulation demonstrated the presence of enhanced electric fields that facilitate the harvesting of carriers and increase the output of the cell. The next step was to add yet another layer in the absorber layer in order to create a more realistic trapezoidal-shaped gradient profile. This model functioned as expected but only reached a peak efficiency of 17.38%. Despite the decrease in efficiency from the dual-graded absorber layer, this result was carried forward since it is a more realistic gradient profile. Following the successful implementation of the trapezoidal absorber layer, we substituted a ZnO buffer layer was substituted for the traditional CdS buffer layer. This step proved to be the most fruitful as it increased the efficiency of the cell to 23.01%, nearly a 4.5% increase. Finally, the inclusion of a top grid created the expected decrease in output, achieving 21.14% efficiency. Overall, the simulations succeeded in modeling a cell that surpasses the current record for Cu(InGa)Se<sub>2</sub> solar cell efficiency.

## **B. RECOMMENDATIONS FOR FUTURE WORK**

Several avenues exist for further work on the research presented in this thesis.

### **(1) Functional Optimization of Absorber Layer**

The models for creating the gradients within the absorber layer of this model were simple functional forms. A detailed functional optimization of the form of the absorber gradient could serve to maximize the output of CIGS cells.

### **(2) Coding of Trap Density Function**

The specification of trap density as a function of Ga concentration was considered, but average trap densities were used for the various regions within the absorber. The development of a C-coded function that can be called from the input file for ATLAS would increase the accuracy of the model for absorbers with graded Ga concentrations.

### **(3) Back Contact Model**

Models for back contact silicon solar cells have been created with results that closely match those of experimentally measured cells. Back contact solar cells eliminate the need for a top grid by aligning the  $p$ - $n$  junction horizontally and placing both contacts on the bottom of the cell. If a CIGS cell can be manufactured using the back contact design, the losses resulting from the top grid can be eliminated and increase the overall output of the cell.

## APPENDIX. SILVACO CODE

```
go atlas

#DEFINE VARIABLES
set ZnO_buffer=.05
set CIGS_thick=1
set ZnO_window=0.2
set MObottom=0.4
set topxcontstart=0.45
set topxcontend=0.55
set topcontht=1
set xcomphigh=0.35
set xcomplow=0.3
set cigs_conc=2e14
set ZnOconc=1e18

# DEFINING MESH (1cm2)
mesh auto width=1e8
x.mesh location=0.0 spacing=.5
x.mesh location=0.4 spacing=.05
x.mesh location=0.6 spacing=.05
x.mesh location=1.0 spacing=.5
# REGIONS
region num=1 material=vacuum y.min=0 y.max=$topcontht
x.min=0 x.max=$topxcontstart
region num=2 material=vacuum y.min=0 y.max=$topcontht
x.min=$topxcontstart x.max=$topxcontend ny=50
region num=3 material=vacuum y.min=0 y.max=$topcontht
x.min=$topxcontend x.max=1
region num=4 material=ZnO bottom thick=$ZnO_window ny=50
region num=5 material=ZnO bottom thick=$ZnO_buffer ny=50
region num=6 material=CIGS bottom thick=$CIGS_thick ny=50
comp.top=$xcomphigh comp.bottom=$xcomphigh
region num=7 material=CIGS bottom thick=$CIGS_thick ny=50
comp.top=$xcomplow comp.bottom=$xcomplow
region num=8 material=CIGS bottom thick=$CIGS_thick ny=50
comp.top=$xcomplow comp.bottom=$xcomphigh
region num=9 material=Mo bottom thick=$MObottom ny=50
conductor

# ELECTRODES
elec num=1 name=cathode material=Aluminum y.min=0
y.max=$topcontht x.min=$topxcontstart x.max=$topxcontend
elec num=2 name=anode bottom
```

```

# DOPING
doping uniform region=4 n.type concentration=$ZnOconc
doping uniform region=5 n.type concentration=$ZnOconc
doping uniform region=6 p.type concentration=$cigs_conc
doping uniform region=7 p.type concentration=$cigs_conc
doping uniform region=8 p.type concentration=$cigs_conc

# SET MATERIAL PROPERTIES
#material region=1 real.index=1.2 imag.index=1.8
#material region=2 real.index=0 imag.index=1000
#material region=3 real.index=1.2 imag.index=1.8
#material TAUN=2e-7 TAUP=2e-7 COPT=1.5e-9 AUGN=8.3e-32
AUGP=1.8e-31

#initial trap information from optimization for a high
efficiency cigs solar cell paper
trap material = CIGS donor e.level=0.9 sign=5e-13 sigp=1e-
15 \
density=1.9e14 y.max=2.32 degen.fac=1
#trap region =5 donor e.level=0.9 sign=5e-13 sigp=1e-15 \
#density=1.2e15 y.max=2.32 degen.fac=1
#trap region =6 donor e.level=0.9 sign=5e-13 sigp=1e-15 \
#density=2.5e15 y.max=2.32 degen.fac=1

#trap info from DLTS characterization paper
#trap material=CIGS donor e.level=0.635 sign=6e-18 sigp=6e-
18
#density=4.2e13 y.max=2.32 degen.fac=1

# MODELS
models srh temperature=300 bound.trap
models optr
models region=6 conmob
models region=7 conmob
models region=8 conmob

# SOLAR LIGHT (AM 1.5)
beam num=1 x.origin=0.5 y.origin=-2 angle=90 am1.5
wavel.start=0.285 wavel.end=1.655 wavel.num=137

# SOLVE I-V CURVE
solve init
solve previous
solve b1=1
log outfile=CIGS_init.log

```

```

solve previous
extract name="Short Circuit current" max(i."cathode")
solve vstep=0.01 vfinal=.2 name=anode \
compliance="$Short Circuit current" cname=cathode
output con.band val.band qfn qfp
save outf=CIGS.str

solve vstep=0.01 vfinal=.4 name=anode \
compliance="$Short Circuit current" cname=cathode
output con.band val.band qfn qfp
save outf=CIGS2.str

solve vstep=0.01 vfinal=.6 name=anode \
compliance="$Short Circuit current" cname=cathode
output con.band val.band qfn qfp
save outf=CIGS3.str

solve vstep=0.01 vfinal=.8 name=anode \
compliance="$Short Circuit current" cname=cathode
output con.band val.band qfn qfp
save outf=CIGS4.str

solve vstep=0.01 vfinal=1 name=anode \
compliance="$Short Circuit current" cname=cathode
output con.band val.band qfn qfp
save outf=CIGS5.str

solve vstep=0.01 vfinal=1.2 name=anode \
compliance="$Short Circuit current" cname=cathode
output con.band val.band qfn qfp
save outf=CIGS6.str

solve vstep=0.01 vfinal=1.3 name=anode \
compliance="$Short Circuit current" cname=cathode

#PLOT THE RESULTS
tonyplot CIGS_init.log
tonyplot CIGS.str CIGS2.str CIGS3.str CIGS4.str CIGS5.str
CIGS6.str

#EXTRACT ADDITIONAL PARAMETERS
extract name="Short Circuit current" max(i."cathode")
extract name="Open Circuit Voltage" x.val from curve
(v."anode," i."cathode") \
where y.val=0

```

```
extract name="Max Power Current" x.val from
curve(i."cathode", ((v."anode")*(i."cathode"))) \
where y.val=max((i."cathode")*(v."anode"))
extract name="Max Power Voltage" x.val from
curve(v."anode", ((v."anode")*(i."cathode"))) \
where y.val=max((i."cathode")*(v."anode"))
extract name="Max Power" max((i."cathode")*(v."anode"))
extract name="FF1" $"Max Power"/($"Short Circuit
Current"*$"Open Circuit Voltage")
extract name="Eff1" $"Max Power"/0.001
quit
```

## LIST OF REFERENCES

- [1] What is operational energy?. (n.d.). Assistant Secretary of Defense for Operational Energy Plans and Programs. [Online]. Available: <http://energy.defense.gov/About.aspx>. Accessed August 3, 2015.
- [2] Department of Defense. (2011, May). Energy for the warfighter: Operational energy strategy. [Online]. Available: <http://www.hqmc.marines.mil/Portals/160/Docs/OEPP%20Strategy.pdf>
- [3] *United States Marine Corps expeditionary energy strategy and implementation plan: "Bases-to-battlefield."* Marine Corps Expeditionary Energy Office, Washington, DC, 2011.
- [4] Global RE opportunity tool (beta). (n.d.). Clean Energy Solutions Center. [Online]. Available: [http://maps.nrel.gov/global\\_re\\_opportunity](http://maps.nrel.gov/global_re_opportunity). Accessed August 3, 2015.
- [5] Ground Renewable Energy System (GREENS) (n.d.). The United States Marine Corps. [Online]. Available: <http://www.marcorsyscom.marines.mil/Portals/105/pdmeps/docs/APS/A0375.pdf>. Accessed August 3, 2015.
- [6] C. Hedelt. (2012, Dec. 20). MCSC helps Marines go green. Marine Corps Systems Command Corporate Communications. [Online]. Available: <http://www.marcorsyscom.marines.mil/News/tabid/5830/Article/136008/mcsc-helps-marines-go-green.aspx>
- [7] A. R. Harvey, "The modification of HOMER software application to provide the United States Marine Corps with an energy planning tool," M.S. thesis, Department of Electrical Engineering, Naval Postgraduate School, Monterey, CA, 2012.
- [8] Equipment in the field. (n.d.). Marine Corps Expeditionary Energy Office [Online] Available: <http://www.hqmc.marines.mil/e2o/Fleet.aspx> Accessed August 3, 2015.
- [9] D. Columbus, "Design and optimization of copper indium gallium selenide solar cells for lightweight battlefield application," M.S.Thesis, Department of Electrical Engineering, Naval Postgraduate School, Monterey, CA, 2014.
- [10] F. Konstantinos, "Modeling and simulation of dual-junction CIGS solar cell using SILVACO ATLAS," M.S. thesis, Department of Electrical Engineering, Naval Postgraduate School, Monterey, CA, 2012.

- [11] M. Iqbal, *An Introduction to Solar Radiation*. New York, NY: Academic Press, 2012.
- [12] B. Richards, “Enhancing the performance of silicon solar cells via the application of passive luminescence conversion layers,” *Solar Energy Mater. Solar Cells*, vol. 90, pp. 2329–2337, 2006.
- [13] S. M. Sze and M. K. Lee, *Semiconductor Devices: Physics and Technology*. 3rd ed. New York, NY: John Wiley & Sons, 2012.
- [14] M. Zeman, *Solar Cells*. 1st ed. Delft, Netherlands: Delft University of Technology, 2005.
- [15] Module IV curve (n.d.). Folsom Labs [Online] Available: [https://www.folsomlabs.com/modeling/module/module\\_model](https://www.folsomlabs.com/modeling/module/module_model) Accessed August 3, 2015.
- [16] A. Luque and S. Hegedus, *Handbook of Photovoltaic Science and Engineering*. 3rd ed., West Sussex, United Kingdom: John Wiley & Sons, 2011.
- [17] S. R. Wenham, “Cell Properties and Design” in *Applied Photovoltaics*. 3rd ed., New York, NY: Earthscan, 2011, pp. 55–65.
- [18] C. S. Solanki, *Photovoltaic technology and systems*. 1st ed., Delhi, India: PHI Learning Private Limited, 2013.
- [19] W. Witte, S. Spiering and D. Hariskos, “Substitution of the CdS buffer layer in CIGS thin-film solar cells,” *Vakuum in Forschung Und Praxis*, vol. 26, no. 1, pp. 23–27, Feb., 2014.
- [20] A. Chirilă, S. Buecheler, F. Pianezzi, P. Bloesch, C. Gretener, A. R. Uhl, C. Fella, L. Kranz, J. Perrenoud and S. Seyrling, “Highly efficient Cu (In, Ga) Se<sub>2</sub> solar cells grown on flexible polymer films,” *Nature Materials*, vol. 10, no. 11, pp. 857–861, 2011.
- [21] X. Ma, D. Liu, L. Yang, S. Zuo and M. Zhou, “Molybdenum (mo) back contacts for CIGS solar cells,” in *Eighth Int. Conf. on Thin Film Physics and Applications*, 2013, pp. 906814-906814.
- [22] M. A. Green, K. Emery, Y. Hishikawa, W. Warta and E. D. Dunlop, “Solar cell efficiency tables (Version 45),” *Progress in Photovoltaics Research Applications*, vol. 23, no 1, pp. 1–9, Jan., 2015.
- [23] R. L. Garris, J. V. Li, M. A. Contreras, K. Ramanathan, L. M. Mansfield, B. Egaas and A. Kanevce, “Efficient and stable CIGS solar cells with ZnOS buffer layer,” in *Photovoltaic Specialist Conference*, 2014, pp. 0353–0356.

- [24] T. Dullweber, O. Lundberg, J. Malmström, M. Bodegård, L. Stolt, U. Rau, H. Schock and J. H. Werner, “Back surface band gap gradings in Cu (In, Ga) Se 2 solar cells,” *Thin Solid Films*, vol. 387, no. 1, pp. 11–13, May, 2001.
- [25] G. Hanna, A. Jasenek, U. Rau and H. Schock, “Influence of the Ga-content on the bulk defect densities of Cu (In, Ga) Se 2,” *Thin Solid Films*, vol. 387, no. 1, pp. 71–73, May 2001.
- [26] S. Song, K. Nagaich, E. Aydil, R. Feist, R. Haley and S. Campbell, “Structure optimization for a high efficiency CIGS solar cell,” in *Photovoltaic Specialists Conference (PVSC)*, 2010, pp. 2488–2492.
- [27] L. Kerr, S. Li, T. Anderson, O. Crisalle, S. Johnston, J. Abushama and R. Noufi, “DLTS characterization of CIGS cells,” in *NCPV and Solar Program Review Meeting Proceedings*, Golden, CO, 2003, pp. 866-869.
- [28] *ATLAS User Manual*, Silvaco, Inc., Santa Clara, CA 2014.

THIS PAGE INTENTIONALLY LEFT BLANK

## INITIAL DISTRIBUTION LIST

1. Defense Technical Information Center  
Ft. Belvoir, Virginia
2. Dudley Knox Library  
Naval Postgraduate School  
Monterey, California